Title

Early steps in reovirus infection are associated with dramatic changes in supramolecular structure and protein conformation: analysis of virions and subviral particles by cryoelectron microscopy and image reconstruction.

Journal

The Journal of cell biology, 122(5)

ISSN

0021-9525

Authors

Dryden, KA
Wang, G
Yeager, M
et al.

Publication Date

1993-09-01

DOI

10.1083/jcb.122.5.1023

Peer reviewed

Early Steps in Reovirus Infection Are Associated with Dramatic Changes in Supramolecular Structure and Protein Conformation: Analysis of Virions and Subviral Particles by Cryoelectron Microscopy and Image Reconstruction

Kelly A. Dryden,* Guoji Wang,* Mark Yeager,‡ Max L. Nibert,§ Keven M. Coombs,§ Deirdre B. Furlong,§ Bernard N. Fields,§ and Timothy S. Baker*

*Department of Biological Sciences, Purdue University, West Lafayette, Indiana 47907; ‡Departments of Cell Biology and Molecular Biology, The Scripps Research Institute, La Jolla, California 92037; and §Department of Microbiology and Molecular Genetics, Harvard Medical School, Boston, Massachusetts 02115

Abstract. Three structural forms of type 1 Lang reovirus (virions, intermediate subviral particles [ISVPs], and cores) have been examined by cryoelectron microscopy (cryoEM) and image reconstruction at 27 to 32-Å resolution. Analysis of the three-dimensional maps and known biochemical composition allows determination of capsid protein location, globular shape, stoichiometry, quaternary organization, and interactions with adjacent capsid proteins. Comparisons of the virion, ISVP and core structures and examination of difference maps reveal dramatic changes in supramolecular structure and protein conformation that are related to the early steps of reovirus infection. The intact virion (~850-Å diam) is designed for environmental stability in which the dsRNA genome is protected not only by tight $\sigma3$-$\mu1$, $\lambda2$-$\sigma3$, and $\lambda2$-$\mu1$ interactions in the outer capsid but also by a densely packed core shell formed primarily by $\lambda1$ and $\sigma2$. The segmented genome appears to be packed in a liquid crystalline fashion at radii < 240 Å. Depending on viral growth conditions, virions undergo cleavage by enteric or endosomal/lysosomal proteases, to generate the activated ISVP (~800-Å diam). This transition involves the release of an outer capsid layer spanning radii from 360 to 427 Å that is formed by 60 tetrameric and 60 hexameric clusters of ellipsoidal subunits of $\sigma3$. The vertex-associated cell attachment protein, $\sigma1$, also undergoes a striking change from a poorly visualized, more compact form, to an extended, flexible fiber. This conformational change may maximize interactions of $\sigma1$ with cell surface receptors. Transcription of viral mRNAs is mediated by the core particle (~600-Å diam), generated from the ISVP after penetration and uncoating. The transition from ISVP to core involves release of the 12 $\sigma1$ fibers and the remaining outer capsid layer formed by 200 trimers of rod-shaped $\mu1$ subunits that span radii from 306 to 395 Å. In the virion and ISVP, flower-shaped pentamers of the $\lambda2$ protein are centered at the vertices. In the ISVP-to-core transition, domains of the $\lambda2$ subunits rotate and swing upward and outward to form a turretlike structure extending from radii 305 to 400 Å, with a diameter of 184 Å, and a central channel 84 Å wide. This novel conformational change allows the potential diffusion of substrates for transcription and exit of newly synthesized mRNA segments. The essence of these orchestrated events is that reovirus is superbly designed to undergo stages of controlled disassembly in which the release of oligomeric protein layers in the outer capsid is coordinated with dramatic protein conformational changes at the icosahedral vertices.

THE examination of steps in viral infection is of fundamental importance in cell biology since such studies provide insight about basic cellular processes. Understanding the replication of simple viral genomes and viral assembly may be relevant to events in eukaryotic cells that are more complex and experimentally less tractable because viruses exploit the cellular machinery. Studies of mammalian reoviruses (family *Reoviridae*) exemplify such a sys-

Address reprint requests to Timothy S. Baker, Department of Biological Sciences, Purdue University, West Lafayette, IN 47907.

Dr. Dryden's present address is Department of Microbiology and Molecular Genetics, Harvard Medical School, Boston, MA 02115.

Dr. Nibert's present address is Institute for Molecular Virology, University of Wisconsin-Madison, Madison, WI 53706.

Ms. Wang's present address is University of Pittsburgh School of Medicine, Department of Pathology, Pittsburgh, PA 15261.

Dr. Coombs' present address is Department of Medical Microbiology, University of Manitoba, Winnipeg, Manitoba, Canada R3E 0W3.

tem: the cell binding and inclusion of reovirus in vacuoles first demonstrated a more ubiquitous receptor-mediated endocytosis phenomenon (Silverstein and Dales, 1968); double-stranded RNA was first identified in reoviruses (Gomatos and Tamm, 1963); and 5′ capping of mRNAs was elucidated with reovirus (Furuichi et al., 1975). Detailed structural information about viral particles and their component proteins is also important for understanding virus–cell interactions and viral pathogenesis. The aim of this study was to examine reovirus virions and subviral particles in order to gain insight into the structural basis of early steps in reovirus infection.

Reoviruses are spherical, nonenveloped viruses ~850 Å in diameter. Two concentric shells of eight structural proteins encapsidate the 10 double-stranded RNA (dsRNA)[1] genome segments, which are grouped in three size classes: large (L), medium (M), and small (S). One segment encodes two polypeptides in alternative reading frames, and the others encode single polypeptides, giving a total of 11 viral proteins ranging in size from 14 to 144 kD (Table I). The proteins are identified with Greek letters which designate the size of the corresponding gene segments: L, *lambda* (λ); M, *mu* (μ); and S, *sigma* (σ). Three nonstructural proteins (μNS, σNS, and σ1s) provide replicative activities within infected cells. (See review by Schiff and Fields, 1990, for additional references.)

Members of the *Reoviridae* are characterized by structural proteins arranged in two or more icosahedral shells. The two capsid layers of mammalian reoviruses are formed by an outer capsid composed of proteins μ1, σ1, and σ3 and a core capsid composed of proteins λ1, σ2, λ3, and μ2. Protein λ2 is thought to span both capsid layers (Table I). Complexes of μ1 and σ3 form the majority of the outer capsid (Weiner and Joklik, 1988) and are arranged with T = 13*l* icosahedral lattice symmetry (Metcalf, 1982). Although most μ1 protein is present in a cleaved form, represented by fragments μ1N and μ1C (Nibert et al., 1991*b*), here we consistently refer to these fragments together as μ1. The μ1 protein was recently proposed to insert into a cellular membrane during penetration early in reovirus infection (Lucia-Jandris, 1990; Nibert et al., 1991*b*). In its structural role, σ3 is necessary for the proper assembly of μ1 (Lee et al., 1981*a*; Tillotson and Shatkin, 1992) and may stabilize the outer capsid in harsh environments (Nibert et al., 1991*a*). Protein σ1 is a minor component of the outer capsid and is located at the icosahedral fivefold vertices as an oligomer (most likely a trimer or tetramer; Strong et al., 1991; Fraser et al., 1990). In some cases, σ1 adopts a highly extended, fibrous conformation >400 Å in length (Furlong et al., 1988; Fraser et al., 1990). Importantly, σ1 serves as the receptor-recognition protein (Lee et al., 1981*b*), and as such is an important determinant of cell tropism in host animals (Weiner et al., 1977). A minor core capsid protein, λ3, appears to be the catalytic component of the viral, RNA-dependent, RNA polymerase (Morozov, 1989), which transcribes the viral gene segments into mRNAs. Pentamers of λ2 manifest guanylyltransferase activity required for adding a 5′ cap to these mRNAs (Cleveland et al., 1986; Seliger et al., 1992). Also, in transcribing particles, λ2 pentamers may form a channel for the exit of newly synthesized mRNA (Bartlett et al., 1974). Functions of the other core capsid proteins (λ1, σ2, and μ2) are poorly characterized. Both λ1 and σ2 exhibit the capacity to bind dsRNA and may thus interact with genomic dsRNA packaged in the particle interior (Dermody et al., 1991). In addition, λ1 includes a sequence motif for binding nucleotide triphosphates, which may be associated with transcription or capping activity (Weiner and Joklik, 1989).

Mammalian reoviruses have two well-defined types of subvirion particles (intermediate, or infectious, subvirion particles [ISVPs], and cores) which result from the loss of different subsets of outer capsid proteins and are proposed to play essential roles in the early steps of infection. ISVPs are characterized by the loss of σ3 via proteolytic degradation and contain both fragments of a secondarily cleaved form of μ1/μ1C (Nibert and Fields, 1992). Protein σ1 also appears to adopt a more extended conformation in ISVPs compared to virions (Furlong et al., 1988). In most cases, ISVPs are fully infectious; they are generated in an extracellular location during infection by the natural, enteric route in mice (Bodkin and Fields, 1989) but can also be generated within late endosomes or lysosomes of cells when virions initiate infection (Sturzenbecker et al., 1987). ISVPs are thought to be required intermediates in infection because they are uniquely capable of initiating penetration of a cell membrane to provide access of virus to the cytoplasm (Lucia-Jandris, 1990; Nibert et al., 1991*b*). Subsequent conversion of ISVPs to core particles results in the loss of σ1 and μ1 (Smith et al., 1969; Joklik, 1972). Notably, pentamers of λ2 are visible in cores as large "spikes," which protrude from the surface (Ralph et al., 1980) along the fivefold axes. Although cores are noninfectious, they are capable of transcribing, capping, and extruding the full-length viral mRNAs (Joklik, 1983). They are generally accepted to be the transcriptionally active form of the virus that occurs after penetration.

The diameter of reovirus is two to three times larger than that of viruses whose structures have been determined at high resolution by x-ray crystallography (Rossman and Johnson, 1989). Although reovirus cores have been crystallized, diffraction was limited to 8-Å resolution (Coombs et al., 1990). CryoEM and three-dimensional image reconstruction offer a powerful, alternative approach to examine the architecture of such large, complex viruses at moderate (20–40 Å) resolutions (Adrian et al., 1984; Baker, 1992). A key benefit of cryoEM compared to traditional microscopy methods is that biological macromolecules can be frozen and examined in defined physiological buffers, thereby maintaining their "native" structures (Unwin, 1986; Chiu, 1986; Dubochet et al., 1988). In addition, conventional techniques like negative staining reveal only solvent-accessible surfaces, whereas microscopy of frozen-hydrated specimens reveals both external and internal features (Taylor and Glaeser, 1976; Jaffe and Glaeser, 1984; Milligan et al., 1984). Computer-based processing of images recorded by cryoEM has permitted the determination of the three-dimensional structures of a wide variety of icosahedral viruses (Baker, 1992).

The feasibility of examining reovirus particles by this approach was recently demonstrated by Metcalf et al. (1991), in which virions of two strains of mammalian reoviruses (type 2 Jones and type 3 Dearing) and cores of one strain (type 3 Dearing) were examined at 30- and 55-Å resolution, respectively. We have used cryoEM and image reconstruc-

1. *Abbreviations used in this paper*: dsRNA, double-stranded RNA; cryoEM, cryoelectron microscopy; T1L-V, T1L-I, and T1L-C, reovirus serotype 1 (Lang) virions, intermediate subviral particles (ISVPs), and cores, respectively.

*Table I. Reovirus Structural Proteins**

Particle(s)	Protein	Gene	Mass (kD)	Copies (virion)	Some functions and properties
Virion	$\sigma 3$	S4	41	600§	Major outer capsid protein Hydrophilic Metalloprotein with Zn-finger motif
Virion, ISVP	$\mu 1$	M2	76	600§	Major outer capsid protein Undergoes a series of proteolytic cleavages **Myristoylated NH_2 terminus
Virion, ISVP	$\sigma 1$	S1	51‡	36‖–48	Cell-attachment protein Viral hemagglutinin Neutralizing antigen Compact and extended conformations
Virion, ISVP, Core	$\lambda 2$	L2	144	60	Pentameric core spike Guanylyltransferase activity
Virion, ISVP, Core	$\lambda 1$	L3	137	120	Major core protein Binds genomic dsRNA Contains NTP binding motif Metalloprotein with Zn-finger motif
Virion, ISVP, Core	$\sigma 2$	S2	47	120‡‡–180	Major core protein Binds genomic dsRNA
Virion, ISVP, Core	$\lambda 3$	L1	142	12	Minor core protein Putative catalytic subunit of viral polymerase
Virion, ISVP, Core	$\mu 2$	M1	83	12	Minor core protein

* Summarized from review by Schiff and Fields (1990), except where noted.
‡ Mass of T1L $\sigma 1$ differs from type 3 Dearing, unlike the other structural proteins.
§ Current report.
‖ Strong et al., 1991.
** Nibert et al., 1991*b*.
‡‡ Coombs et al., 1990.

tion to examine all three recognized particles (virions, ISVPs, and cores) of a third strain of mammalian reoviruses, type 1 Lang (T1L), and determined the three-dimensional structures of each at resolutions of 27 to 32 Å. Our study considerably extends the analysis of the complex supramolecular organization of reovirus particles from that of Metcalf et al. (1991), primarily because we have included the ISVP, which is intermediate between virions and cores. The new results provide information about the location, shape, size, quaternary arrangement, and stoichiometry of the viral proteins, and the liquid crystalline packing of the dsRNA genome. Comparisons of the three structures also suggest structural alterations (e.g., protein losses and conformational changes) that are relevant to early steps in reovirus infection.

Materials and Methods

Sample Preparation

Cells and Viruses. Spinner-adapted mouse L929 cells were grown in either monolayer or suspension cultures in Joklik minimal essential medium (Irvine Scientific, Santa Ana, CA) supplemented with 2.5% FCS (Hyclone Laboratories, Logan, UT), 2.5% viable serum protein (Biocell Laboratories, Carson, CA), 2 mM glutamine (Irvine Scientific), and 100 U of penicillin and 100 μg streptomycin per milliliter. Stocks of T1L-V (the prototype of serotype 1) were grown and titered in mouse L929 cell monolayers as previously described (Tyler et al., 1985).

Virus Purification. L929 cells at a concentration of 2×10^7/ml were inoculated with second-passage viral cell lysate stocks at a multiplicity of infection of 5 to 10 plaque-forming units per cell as described (Furlong et al., 1988). Infected cells were diluted to a concentration of 6×10^5/ml in suspension cultures and grown for 60 h at 34°C. After incubation, cells were harvested by low-speed centrifugation (1,000 rpm; IEC CRU-5000) resuspended in ice-cold homogenization buffer (250 mM NaCl, 10 mM β-mercaptoethanol, 10 mM Tris, pH 7.4) supplemented with 0.25 mM solid PMSF (Sigma Chemical Co., St. Louis, MO), 0.5 μg/ml pepstatin A, 0.5 μg/ml leupeptin, and 1% (wt/vol) aprotinin (Virgin et al., 1991), freeze-thawed, and freon-extracted twice, as previously described (Smith et al., 1969; Furlong et al., 1988). The final aqueous phases were layered onto chilled, preformed 1.25 to 1.45 g/ml cesium chloride gradients and spun at 23,000 rpm for at least 4 h in a rotor (SW28.1; Beckman Instruments, Palo Alto, CA); maintained at 5°C. The visible virus band at a density of 1.36 g/ml was collected, diluted with virus dialysis buffer (D Buffer: 150 mM NaCl, 15 mM $MgCl_2$, 10 mM Tris, pH 7.4), repurified in a second cesium chloride gradient, and then dialyzed extensively against D Buffer. Aliquots of native virus were then dialyzed against HMN Buffer (10 mM Hepes [Sigma Chemical Co.], 20 mM $MgCl_2$, 125 mM NaCl, pH 8.0).

Generation and Purification of Subvirion Particles. The concentration of purified, native virus dialyzed against D buffer was measured by optical density, using the relationship: 1 $ODU_{260nm} = 2.1 \times 10^{12}$ virus particles per milliliter (Smith et al., 1969). Virus concentration was adjusted to 1×10^{13}/ml for T1L-I preparations; or adjusted to 6×10^{13}/ml for T1L-C. Tosyllysine chloromethyl ketone-treated α-chymotrypsin (Sigma Chemical Co.) was added at 200 μg/ml, and virus was digested at 37°C as described (Borsa et al., 1973; Nibert and Fields, 1992). The reactions were terminated at 1 h for T1L-I and 3 h for T1L-C by adding PMSF to 2.5 mM and chilling on ice. Subsequent manipulations were carried out at 5°C. T1L-I and T1L-C samples were first purified by rate-zonal centrifugation at 25,000 rpm for 75 min in 10 to 40% (wt/vol) sucrose gradients in a rotor (SW28.1; Beckman Intruments) and then by density centrifugation in 1.25 to 1.55 g/ml

cesium chloride gradients at 25,000 rpm for 3 h in a SW28.1 rotor. TIL-I and TIL-C samples were divided into two sub-samples, and the paired samples were dialyzed in parallel. TIL-I was dialyzed against D Buffer and then HMN Buffer, and TIL-C was dialyzed against Core Buffer (1 M NaCl, 100 mM $MgCl_2$, 25 mM Hepes, pH 8.0). One member of each parallel series was used to determine the particle concentration, and to confirm particle identities by negative stain transmission EM and protein composition by SDS-PAGE. Particle concentration was determined by optical density; for TIL-V: 1 ODU_{260nm} = ~0.39 mg/ml virus; for TIL-I: 1 ODU_{260nm} = 2.7 × 10^{12} (~0.39 mg/ml virus); and for TIL-C: 1 ODU_{260nm} = 4.35 × 10^{12} (~0.25 mg/ml virus) (Coombs et al., 1990). The other dialyzed member of each parallel series was then used for cryoEM.

Cryoelectron Microscopy

Samples were prepared for cryoEM by applying ~4 μl of each specimen (~1 mg/ml) to holey-carbon films on 400-mesh copper grids, blotting with filter paper, and immediately plunging into ethane slush (Dubochet et al., 1988; Yeager et al., 1990). Cowpea mosaic virus, mixed with one of the TIL-C samples, served as an internal calibration standard (Olson and Baker, 1989; Belnap et al., 1993). Conditions for cryoEM are summarized in Table II. Images of TIL-V and TIL-I were recorded at a nominal magnification of 30,000×, whereas TIL-C images were recorded at ~36,000× (Table II). TIL-V and TIL-I particles often assumed preferred orientations in the vitrified sample on the grid. To obtain a suitable data set for three-dimensional analysis, images were recorded with the grid tilted 7° or 10° in the microscope, which provided a more random distribution of views.

Core particles were maintained in a buffer with a high salt concentration to prevent aggregation. CryoEM of the sample in Core Buffer, however, routinely resulted in specimens embedded in ice that were too thick for transmission microscopy. Interestingly, specimens stained with uranyl acetate did not display significant aggregation. To minimize aggregation, virus specimens were prepared at high concentration (~25 mg/ml). An aliquot was then diluted 1:10 with water just before application to the grid. Blotting and freezing were carried out as described above. Although some particle aggregation still occurred, a sufficient number of individual cores could be identified for image processing. Visual inspection showed that this rapid dilution technique did not appear to cause particle disruption or detectable changes in size or morphology.

Image Processing and Three-Dimensional Reconstructions

All micrographs were digitized at 25-μm sampling intervals on a microdensitometer (Optronics International, Inc., Chelmsford, MA; or Perkin-Elmer Corp., Eden Prairie, MN). Particles clearly separated from neighbors or background contamination were selected and masked as individual images. The image intensity values were adjusted to remove linear background gradients (Booy et al., 1991) and to normalize the means and variances of the data (Carrascosa and Steven, 1978). We refined the translation (x,y) and orientation (θ,ϕ,ω) parameters for each particle by use of repeated cycles of common-lines, cross-common lines, and correlation procedures (Fuller, 1987; Baker et al., 1988, 1990, 1991). Three-dimensional reconstructions were computed from the "best" particle images in each data set (Table II) according to criteria described by Crowther (1971). Several tests were used to identify and eliminate images that were inconsistent with the entire data set. Images were typically discarded if they showed poor correlation with the expected icosahedral symmetry (Crowther, 1971), if they differed significantly (>10°) from the mean data as measured by the cross-common lines phase error (Fuller, 1987), or if they had a correlation coefficient, calculated between the raw image and the corresponding projected view of an intermediate reconstruction, greater than one standard deviation below the mean coefficient of the entire data set.

To quantitatively assess the resolution limits of the TIL-V and TIL-I data sets, we first computed two independent reconstructions of each particle and compared the respective three-dimensional data sets by use of the R factor (Baker et al., 1991) and correlation coefficient tests (Press et al., 1989). Before computing the reconstructions, we randomly subdivided the images in each of the TIL-V and TIL-I data sets into two smaller data sets so that refinement of orientation and translation parameters could be carried out independently for each subset. After we determined the resolution limits for the TIL-V and TIL-I data, all images of each particle type were combined to compute the final three-dimensional reconstructions (Table II). For TIL-V, images from two different micrographs, corresponding to specimens tilted by 0° and 7°, were combined (Table II) after correcting for slight differences in magnification.

The comparatively small size of the TIL-C data set precluded analysis of the resolution limit for this particle as described for TIL-V and TIL-I. Instead, after computing the final TIL-C reconstruction, the TIL-C data set was randomly divided into two unique subsets that were separately refined for one cycle and then used to compute two independent reconstructions for assessing the resolution. The orientations of particles in the TIL-C data set were more difficult to refine compared to the other data sets for at least two reasons. First, the less-defocused TIL-C micrograph had significantly lower contrast, which made particle features (especially enantiomorphic ones) in different views more difficult to distinguish. Secondly, the TIL-C specimen was diluted tenfold immediately before cryo-preservation in order to maintain optimal ice thickness (see above). The rapid change in ionic strength may have caused slight structural or background fluctuations not detected by visual inspection of the micrographs.

Because reovirus particles tend to assume preferential orientations, an eigenvalue spectrum was computed for each of the three data sets at the respective resolution limits given in Table II. This spectrum provides a test for the presence of errors generated in reconstructions from a nonrandom distribution of particle orientations (Crowther et al., 1970). In each instance, all eigenvalues exceeded 1.0, and >99% of the eigenvalues exceeded 10.0 (Table II). The completeness of the data used to compute each of the three reconstructions was therefore clearly established.

The magnification of the TIL-C micrograph (Table II) was calibrated by use of the cowpea mosaic virus internal standard (Olson and Baker, 1989; Belnap et al., 1993). The magnifications of the TIL-V and TIL-I micrographs (Table II) were then calibrated against the TIL-C micrograph by assuming that the position of the peak density, corresponding to the shell of the core capsid, was invariant in radial density plots. This assumption is supported by the identical arrangement of density features spanning the radii of the core capsid in all three reconstructions. We calculated correlation coefficients between the raw data and projected images of the reconstructions to further refine and correct (by reinterpolation of the image data) small deviations of ~1% or less in the magnifications of individual particle images. Reconstructions computed from reinterpolated data were then used for additional cycles of data refinement. The final density maps were symmetry averaged to impose the full icosahedral (532) point group symmetry (Fuller, 1987).

All calculations were performed with FORTRAN programs (Fuller, 1987; Baker et al., 1988) operated on a microVAX II or a VAX/VMS 8550 computer (Digital Equipment Corp., Maynard, MA) equipped with a RISC co-processer (Vaccelerator model AP/30; Avalon Computer Systems, Santa Barbara, CA). Images were generated, displayed, and photographed on raster graphics devices as previously described (Baker et al., 1991). The threshold contour levels chosen for rendering surface-shaded representations of the three-dimensional maps were typically set at a density value three to four standard deviations of the noise level above the average noise in the map. The noise level was determined from the variation in density values at a radius beyond the defocus fringe outside the particle. The data presented here were not corrected for the effects of the contrast transfer function of the microscope (Toyoshima and Unwin, 1988). Preliminary corrections of the reconstructed density maps did not alter the data in a way that significantly changed the appearance of the maps or our interpretations.

Results

Cryoelectron Microscopy

Micrographs of unstained, frozen-hydrated samples of TIL-V, TIL-I, and TIL-C reveal three distinct particles, all with an approximate circular perimeter but each with a unique morphology and size (Fig. 1).

TIL-V, the largest of the reovirus particles (~850-Å diam), exhibits some views in which the profile is clearly non-circular because portions of the particle periphery appear somewhat flattened or concave (Fig. 1 *A*, *arrows*). This feature is consistent with the divot-like depressions previously observed in negatively stained samples (Furlong et al., 1988). Most TIL-V particles also have a white (electron translucent) ring at a radius of ~290 Å and what appear as short (~80 Å), fingerlike projections at the periphery. TIL-I (~800-Å diam) shows a similar ring at a radius of ~290 Å and also distinct regions at the periphery consisting of either

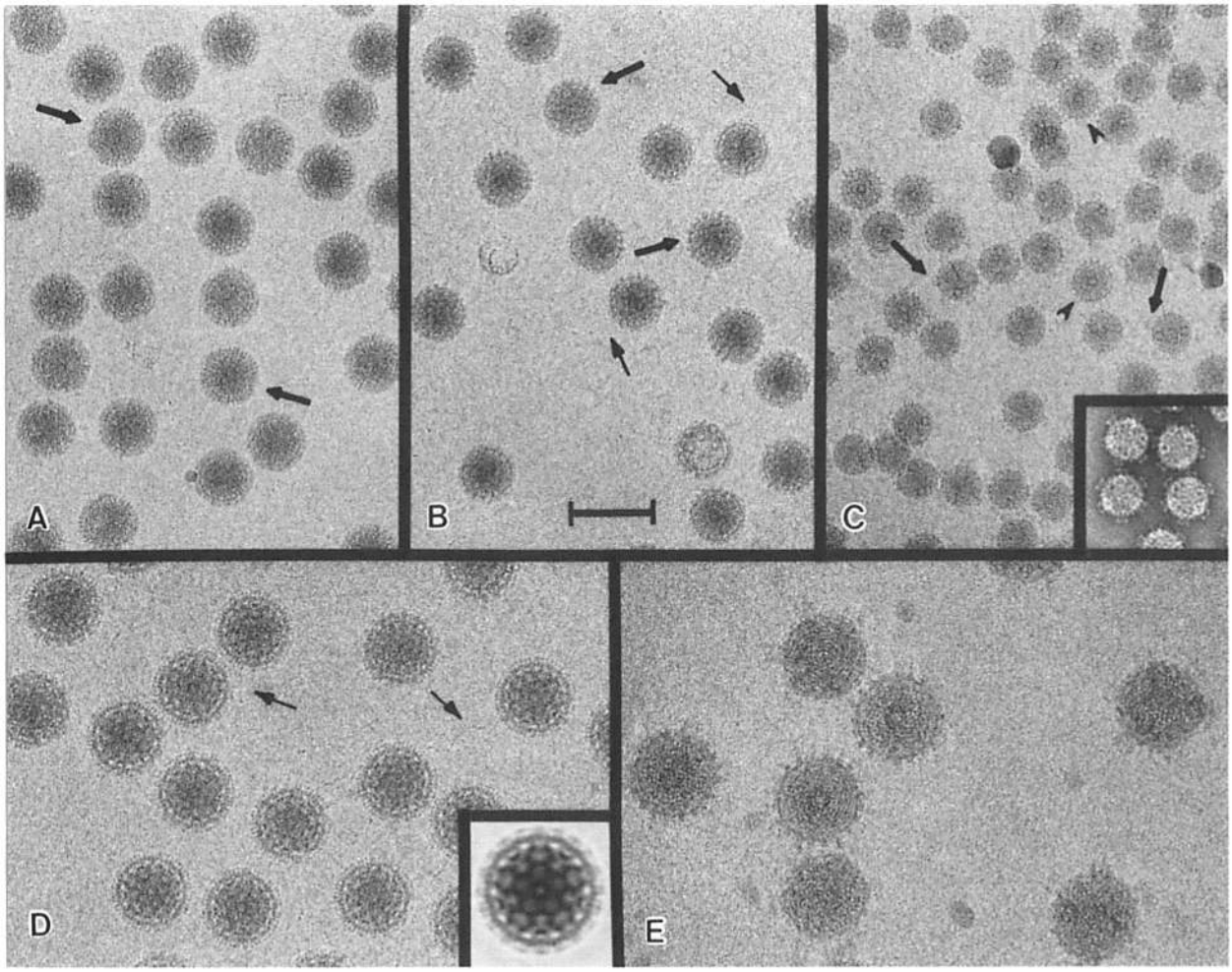

Figure 1. Images of frozen-hydrated reovirus virions and subviral particles by minimal-dose cryoEM (type 1 [Lang] virions [*A*], intermediate subviral particles [*B*], and cores [*C*]). Arrows in A identify flattened profiles in T1L-V, similar to depressions noted in negatively-stained samples (Furlong et al., 1988). Arrows in *B* identify coarse, peripheral features in T1L-I particles. Thin arrows in *B* and *D* identify filamentous projections on T1L-I particles. Arrows in *C* identify large peripheral T1L-C surface spikes, clearly visualized in samples stained with 1% uranyl acetate (*inset*) and arrowheads indicate particles oriented on a fivefold symmetry axis. The frozen-hydrated T1L-I sample (*D*) clearly reveals the preferential (fivefold) orientation of the particles. An average of 38 rotationally aligned particles confirms this preferred orientation (*inset*, 1.5 × enlarged). Close-to-focus images of T1L-C particles (*E*) display a fingerprint striation pattern which we attribute to closely packed RNA. Conditions of microscopy for each image are summarized in Table II. Bar: (*A–C*) 1,000 Å; (*D*) 750 Å; (*E*) 500 Å.

coarse or fine features (Fig. 1 *B*, *arrows*). In addition, some T1L-I particles have filamentous projections that extend up to 400 Å beyond the outer surface (Fig. 1, *B* and *D*, *thin arrows*). These filaments, or fibers, are similar to those seen in negatively stained samples and have been attributed to the σ1 protein (Furlong et al., 1988). Careful examination of the less defocused T1L-C micrograph reveals large protrusions that extend outside the periphery of the ~600-Å-diam particle (Fig. 1 *C*, *arrows*). The protruding spikes are more clearly visualized in negatively stained samples (White and Zweerink, 1976; Fig. 1 *C*, *inset*) or in images of frozen-hydrated samples recorded much farther underfocus (Metcalf et al., 1991). These protrusions appear donutlike when two spikes on opposite surfaces of a core particle are superimposed and viewed end-on down a fivefold symmetry axis (Fig. 1 *C*, *arrowheads*).

Initial micrographs of T1L-I revealed that, for a given field of view, most particles adopted a preferred orientation (Fig. 2), with either a fivefold (Fig. 1 *D*) or a threefold (data not shown) axis parallel to the direction of view. The preferred fivefold orientation is clearly revealed in an average of many particle images (Fig. 1 *D*, *inset*), whose features (e.g., pentagonal flowerlike structure in the center of the particle and fingerlike projections around the entire periphery of the particle) are also apparent in each of the unprocessed images (Fig. 1 *D*). Samples of T1L-V also showed a tendency to preferentially orient. Therefore, to compute the three-dimensional structures of T1L-V and T1L-I to moderate (<30 Å) resolution, it was necessary to record images with the microscope specimen stage tilted in order to generate a satisfactory distribution of unique projected views (Fig. 2, Table II). Although T1L-C did not preferentially orient (Fig. 1 *C*), the particles tended to aggregate at reduced ionic strength (Coombs et al., 1990) which limited the number of particles in any single image that could be used for image processing. Highly magnified, close-to-focus views of T1L-C also exhibited striated whorls, resembling "fingerprints," in the particle images (Fig. 1 *E*).

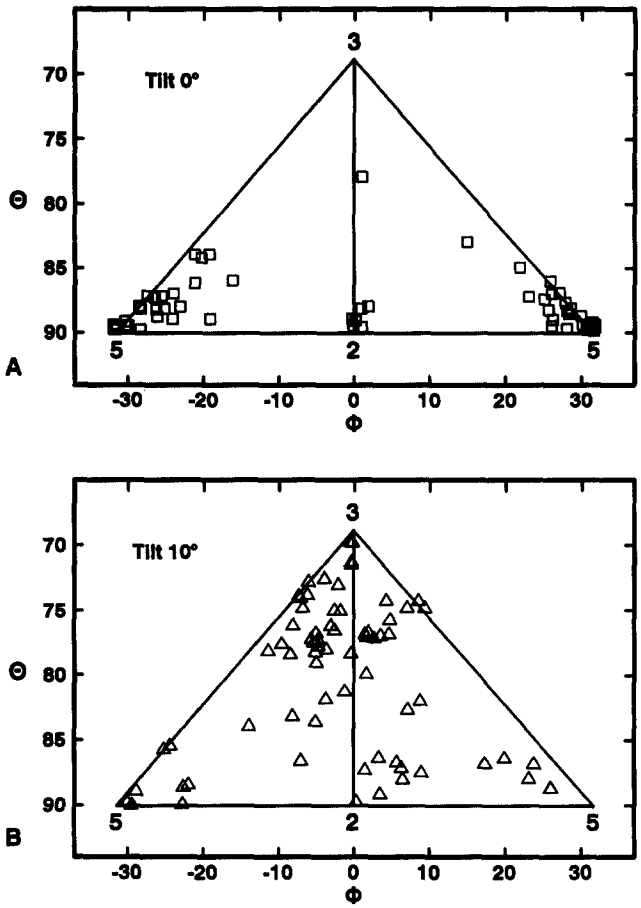

Figure 2. Plots of refined orientation angles for T1L-I images recorded at specimen tilts of 0° (*A*) or 10° (*B*). Particles in the untilted specimen display preferential orientation along a fivefold axis of symmetry as is evident in the unprocessed image (Fig. 1 D). Tilting by 10° provides a more random distribution of unique views, thereby allowing interpolation of the three-dimensional Fourier transform and computation of the three-dimensional density map by Fourier-Bessel inversion. Note that B represents a specimen in which many T1L-I particles were preferentially oriented along a threefold axis of symmetry.

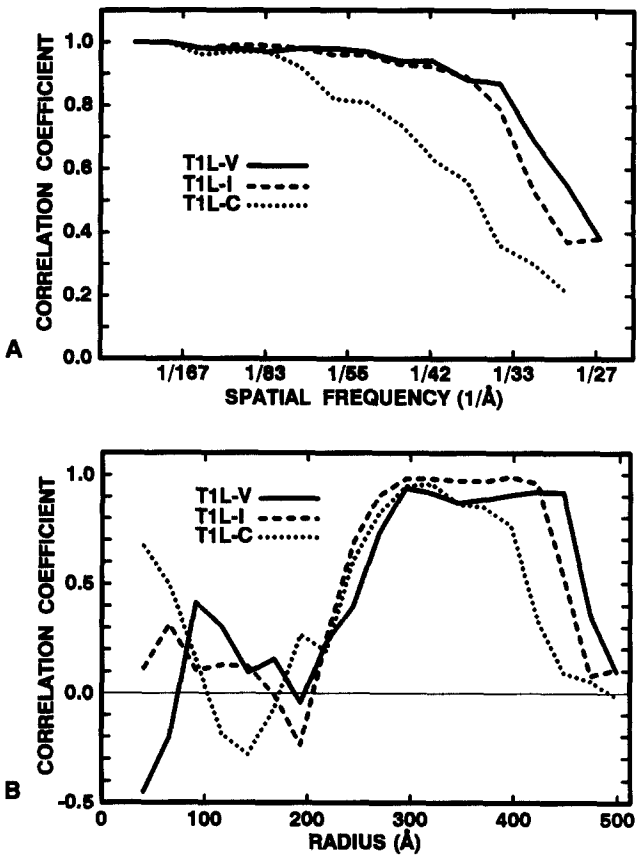

Figure 3. Correlation coefficient analysis of reovirus data. The T1L-V, T1L-I, and T1L-C image data were randomly divided, and two independent reconstructions were computed for each type of particle. Independent reconstructions were compared pairwise as a function of spatial frequency (*A*) and radius (*B*). Perfectly matched data would have a correlation coefficient of 1.0, whereas random data would have a correlation coefficient of 0.0. The resolution limits determined from these plots for the T1L-V, T1L-I, and T1L-C reconstructions are ~28, ~29, and ~35 Å (*A*), respectively. The highest correlation coefficients in *B* identify the location of icosahedrally organized protein shells.

Image Processing

The micrographs of T1L-V, T1L-I, and T1L-C were digitized, and the best images of each particle type were refined to determine phase origins and relative orientations for computation of three-dimensional reconstructions (Table II). The resolution limit of each data set was quantitatively assessed by tests in both real and reciprocal space conducted on independent reconstructions computed for each particle form (Fig. 3). Correlation coefficients, computed as a function of spatial frequency between pairs of reconstructions (Fig. 3 *A*), indicate that the resolution limits (judged to occur at a coefficient of 0.5) of the T1L-V and T1L-I data are at ~28 and 29 Å, respectively, whereas the T1L-C data set is limited to ~35-Å resolution. These limits are conservative estimates because the final reconstructions were computed from data sets twice as large as those required for these calculations (Baker et al., 1991). Therefore, the final reconstructions of T1L-V, T1L-I, and T1L-C were computed to resolution limits of 27.0, 28.0, and 32.0 Å, respectively, from data sets that included 88, 86, and 28 independent particle images (Table II). The radial dependence of the correlation coefficient (Fig. 3 *B*) shows that the regions of the T1L-V, T1L-I, and T1L-C maps that are statistically most reliable correspond to the protein shells (radii ranging from ~250 to ~395–425 Å). The nucleic acid region (radii <230 Å) and the external solvent regions (radii >395–425 Å) display the lowest correlations. These observations indicate that the protein shells are organized with a high degree of icosahedral symmetry, whereas the nucleic acid and solvent regions are not.

To compute reovirus reconstructions reliably to 25–30-Å resolution, images of particles in many different orientations had to be combined and averaged. For T1L-V, we combined data from two separate micrographs, from a tilted and an untilted specimen. The relative magnifications of the two T1L-V micrographs were determined so the data from each could be scaled before the initial refinement steps. The quality of reconstructions markedly improved if variations in micrograph magnifications were corrected. In addition, we found, as have others (Aldroubi et al., 1992), that the relative size

Table II. Microscopy and Image Analysis Data

Specimen	T1L-V		T1L-V	T1L-I	T1L-C
Microscope*	EM420		EM420	EM420	CM-12
Voltage (kV)	80		80	80	100
Nominal magnification	30,000		30,000	30,000	35,000
Calibrated magnification	29,500		30,200	27,700	35,700
Objective lens defocus (μm)	1.0		1.0	1.0	0.5
Electron dose ($e^-/Å^2$)	6		6	6	10
Goniometer setting	0°		7°	10°	0°
Digital image pixel size (Å)	8.5		8.3	9.0	7.0
Image box size (pixels)	127^2		121^2	127^2	123^2
Number of images boxed	95		64	98	54
Number used in reconstruction	(44)	88	(44)	86	28
Percent Eigenvalues‡ 100–∞		95.3		98.7	75.0
10–100		4.6		1.3	25.0
1–10		0.1		0.0	0.0
Resolution limit (Å)§		27.0		28.0	32.0
Correlation coefficient‖		0.82		0.87	0.79

* Philips Electron Instruments, Mahwah, NJ.
‡ Average of real and imaginary components; computed to resolution limit specified for each reconstruction.
§ Resolution cut-off used to calculate each reconstruction.
‖ Computed between original images and corresponding back-projections of the reconstruction.

of particles within the same image varied by ~1%. Thus, we rescaled the individual images to maximize the correlation coefficients computed between them and the corresponding projected views of an interim reconstruction. A new reconstruction was then computed and used for another cycle of refinement of magnification scale factors. The average correlation coefficients for each of the rescaled data sets with respect to the three final reconstructions were 0.82, 0.87, and 0.79 (<0.02 standard deviations for all three) for the T1L-V, T1L-I, and T1L-C data, respectively (Table II).

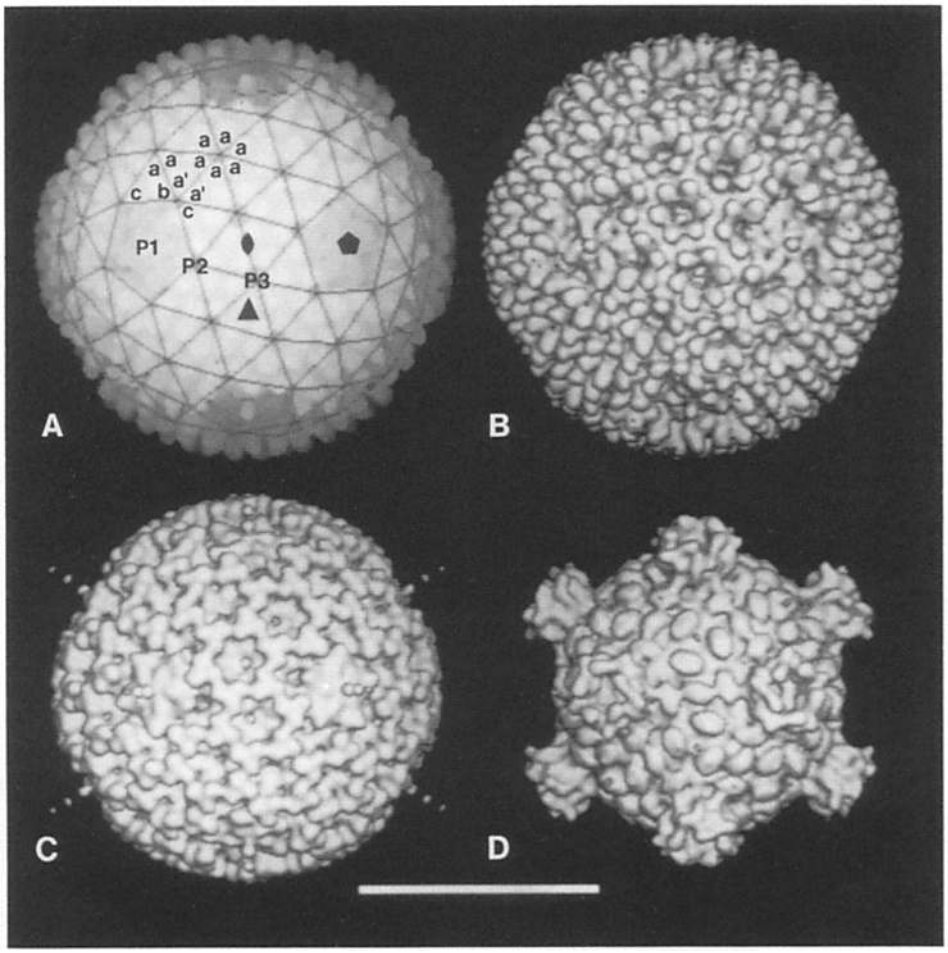

Figure 4. Surface-shaded representations of reovirus reconstructions viewed down a twofold axis of symmetry. The T = 13 (laevo) icosahedral lattice symmetry and P1, P2, and P3 lattice positions are displayed in *A* (nomenclature of Metcalf et al., 1991). The 120 hexa-coordinated points are distributed among two classes: 60 P2 points are nearest the P1 penta-coordinated sites, and 60 P3 points are nearest the icosahedral threefold symmetry axes. Equivalent subunits nearest a P3 position are identified with the letter *a*. The four subunits at each P2 position occupy two identical (*a'*) and two nonidentical (*b* and *c*) positions. T1L-V (*B*) is characterized by 600 fingerlike projections and 12 depressions containing five-petalled, flower-shaped features at the fivefold vertices. T1L-I (*C*) has similar flowerlike features centered on the icosahedral vertex positions from which thin, beaded, spikelike features extend an additional ~110Å. The flower-shaped features in T1L-V (*B*) and T1L-I (*C*) are located at the 12 penta-coordinated P1 positions at the fivefold axes. T1L-C (*D*) is notable for its knobby morphology and the 12 turretlike features centered at the fivefold vertex positions. Bar, 500 Å.

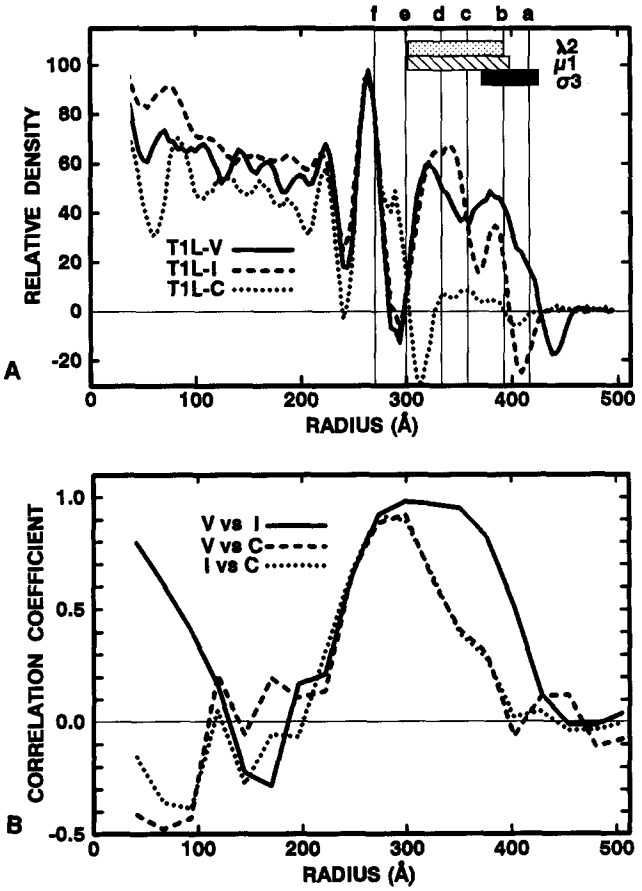

Figure 5. Plots of radial density and cross-wise correlation for reovirus reconstructions. (*A*) Plots of the spherically averaged density as a function of radius for the T1L-V, T1L-I, and T1L-C reconstructions. The icosahedrally arranged outer protein shell in the intact virion (T1L-V) spans radii of 305 to 427Å. RNA is concentrated at radii <230Å. The densities at radii of 415, 390, 360, 335, 300, and 270Å (*a–f*) are displayed as projection density maps in Fig. 6. Based on the interpretation of the density maps, proteins $\sigma 3$, $\mu 1$, and $\lambda 2$ span radii as indicated. Density plots were scaled to the same relative magnification by assuming that the peak density in the T1L-C map (270-Å radius) was invariant in the three particles. (*B*) Correlation coefficient plotted vs. radius for the three possible pairwise comparisons of the T1L-V, T1L-I, and T1L-C reconstructions, which can be used to identify regions of comparable density in the three particles. The high correlation coefficient values for radii between 250 and 320 Å indicate comparable mass density for the three particles at these positions.

Surface Features of Reovirus Particles

Surface-shaded representations of the three reconstructions clearly reveal the external similarities as well as the differences between particle forms (Fig. 4). The internal features of each reconstruction were also examined by means of radial density plots (Fig. 5) and projection density maps at defined radii (Fig. 6), which provide a basis for understanding relationships between morphological subunits.

Icosahedral Lattice. The outer capsids of T1L-V and T1L-I both have morphological subunits arranged on an incomplete T = 13(laevo) icosahedral surface lattice (Fig. 4 *A*). The absolute hand of the reovirus surface lattice was previously determined from images of virions that were freeze-etched and shadowed (Metcalf, 1982) or unevenly (single-sided) stained (Khaustov et al., 1987). After the nomenclature of Metcalf et al. (1991), a strict T = 13 lattice has 12 penta-coordinated (P1) points at the fivefold icosahedral vertices and 120 hexa-coordinated points distributed among two classes, with 60 P2 points nearest the penta-coordinated sites and 60 P3 points nearest the icosahedral threefold axes of symmetry. A strict T = 13 structure, with chemically identical subunits arranged according to the principles of viral assembly as envisioned by Caspar and Klug (1962), would have 780 (= 12 × 5 + 120 × 6) quasi-equivalently related subunits. The reovirus structures clearly do not conform to these strict rules (Fig. 4) because the surface features around the P1 positions are very different morphologically from those around the P2 and P3 positions. Nevertheless, the reconstructions show that much of the outer capsid is composed of subunits that are symmetrically packed as if part of a complete T = 13 structure.

Mature Virion (T1L-V). The maximum diameter of the T1L-V shell is 855 Å, which compares favorably with the 830-Å dimension obtained by small-angle, x-ray solution scattering (Harvey et al., 1981). The most prominent features on the external surface of the virion are 600 fingerlike projections (subunits) and a flower-shaped structure in a depression at each of the 12 icosahedral fivefold axes (Fig. 4 *B*). Each subunit extends ~34 Å above the main shell of the outer capsid and is ~36 Å in diameter. The 600 subunits are arranged as 60 P3-hexamers (60 × 6 = 360 subunits) and 60 P2-tetramers (60 × 4 = 240 subunits). Each P3-hexamer encircles a 42-Å-diam hole that forms an opening into a solvent channel that extends radially inwards. The P2-tetramer consists of four subunits, arranged as if part of an incomplete hexamer, whose two subunits nearest the P1 positions are missing. The four P2 subunits are in three distinct environments (see labels of Fig. 4 *A*): the two furthest from the fivefold axes (a') are in a packing environment that appears to be identical to the P3 subunits (a), whereas the other P2 subunits appear to be unique (b and c), with one (b) in close contact with the flower-shaped feature in the large cavity. Because there are also no pentameric aggregates of these subunits at the P1 positions, there are a total of 15 "missing" subunits at each vertex (five at the P1 position and 10 at the five P2 positions) for a total of 180 missing subunits per virion. The absence of these subunits generates the large, open depressions at the fivefold axes and is responsible for the somewhat ovoid particle profile in the twofold orientation (Fig. 1 *A*, *arrows*). At the base of each depression (radius ~370 Å) lies a left-handed, flower-shaped feature with five 90-Å-long petals and a small knoblike density (29 Å in diameter and 46-Å high) extending radially from the center (Fig. 4 *B*). The close correspondence between the outer surfaces of T1L-V (Fig. 4 *B*) and virions of type 2 Jones or type 3 Dearing (Metcalf et al., 1991) suggests that viral particles from different serotypes are indistinguishable at ~30-Å resolution, as expected from the significant amino acid sequence homology of the same proteins from these different serotypes (Weiner and Joklik, 1988; Seliger et al., 1992).

ISVP (T1L-I). T1L-I and T1L-V are easy to distinguish because the overall diameter of the T1L-I shell is smaller (795 Å), the 600 fingerlike subunits seen in T1L-V are absent (consistent with the loss of $\sigma 3$; Table I), and there are 200 trimeric morphological units on the surface (Fig. 4 *C*). 20 of these trimeric units are centered on the strict threefold

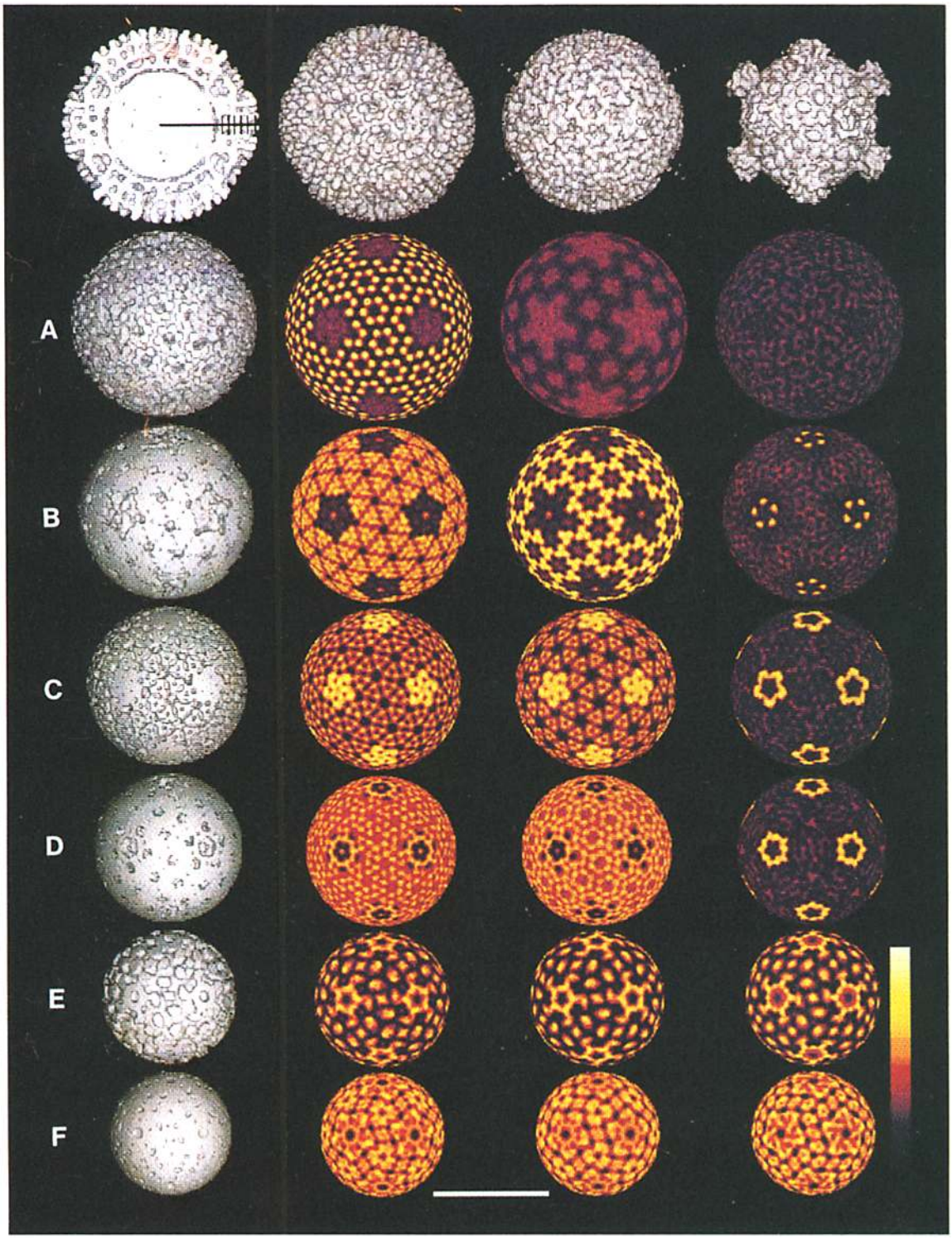

Figure 6. Surface-shaded views (*top row* and *left column*) and projected density maps are truncated at defined radii (*a–f*) of 415, 390, 360, 335, 300, and 270 Å (see Fig. 5) for the TlL-V, TlL-I, and TlL-C reconstructions. The back half of the TlL-V reconstruction (*top left*) is marked to show the progression of views at decreasing radii and the corresponding surface-shaded views are of TlL-V (*left column*). The color table displays density values from lowest (*black*) to highest (*white*). Bar, 500 Å.

axes, and the remaining 180 are centered on local threefold axes of symmetry. Near the surface, each trimeric unit is ~62 Å on a side and consists of three globular subunits of ~28-Å-diam. Of the 600 subunits in the 200 trimers, 540 each appear to make one intertrimer and two intratrimer contacts at high radius (~380–390 Å). The remaining 60 subunits, nearest the P1 positions (on the *b–c* line in Fig. 4 *A*), only form intratrimer contacts. The trimers are arranged

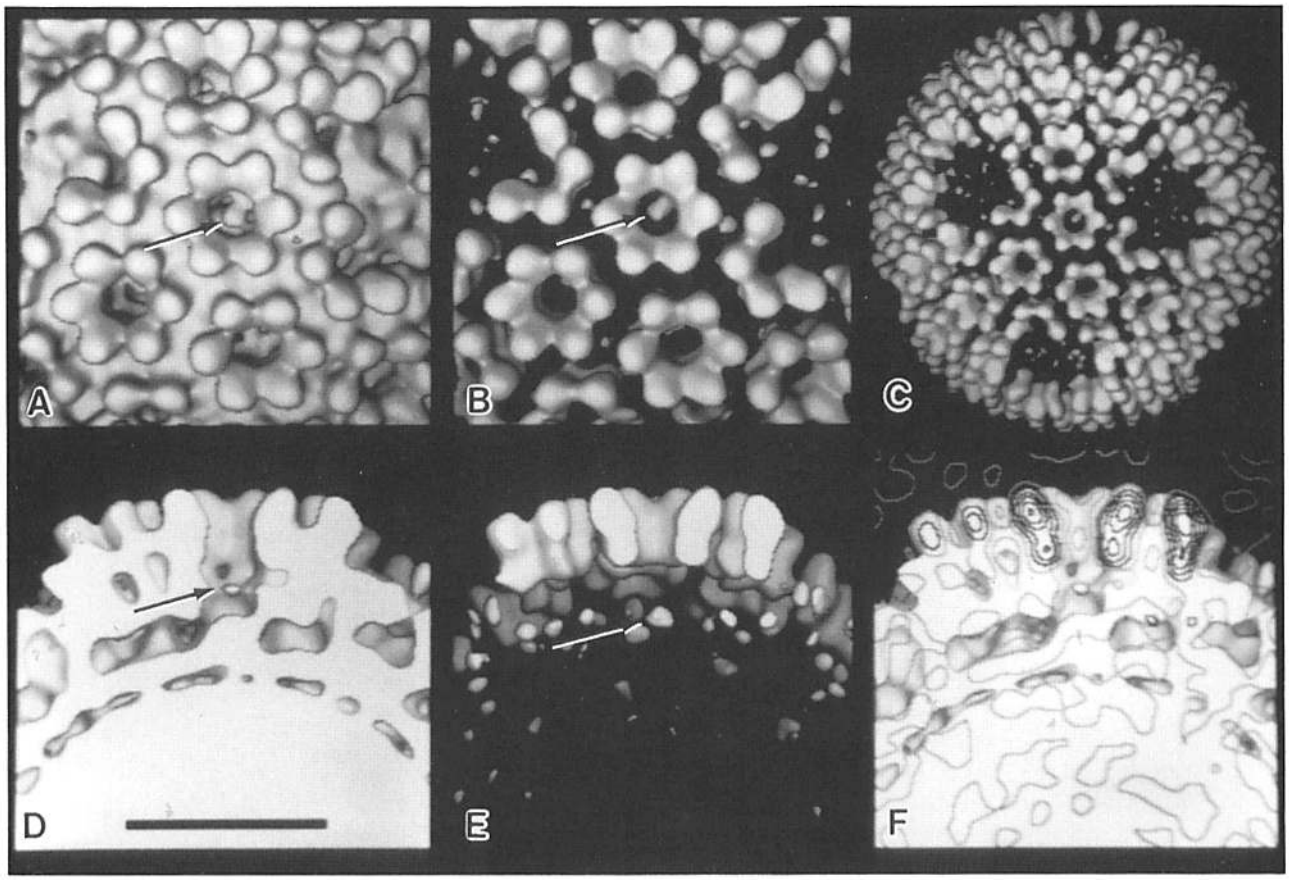

Figure 7. Surface-shaded views of the T1L-V and difference (T1L-V − T1L-I) maps. Close-up top (*A*) and side (*D*) views of the T1L-V surface-shaded map centered along the P3 channel. Corresponding views of the T1L-V − T1L-I difference map are shown in *B* and *E*. The entire difference map is displayed in *C* (855-Å diam). In *F*, a contour plot of the difference map is superimposed on the T1L-V surface view. Black and light grey contours respectively correspond to positive and negative density values. Arrows in the T1L-V map (*A* and *D*) and in the difference map (*B* and *E*) identify two features <20 Å in diameter whose chemical interpretation is uncertain. Bar, 200 Å.

in a discontinuous honeycomb with 60 hexagonal cavities at the P3 positions (external diameter 80–110 Å) that funnel down to 25-Å-diam solvent channels at lower radii (~330 Å). These solvent-accessible channels are in radial register with holes in the surface of T1L-V (Fig. 4, *B* and *C*). A flowerlike feature at each fivefold vertex, with petals in a left-handed arrangement, appears similar in morphology and size to that in T1L-V. But, in T1L-I, a discontinuous fiber of density extends ~110 Å out from the center of the flower along the fivefold axis to a maximum radius of 480 Å.

Core (T1L-C). The knobby external morphology of T1L-C clearly differentiates this viral particle from T1L-V and T1L-I particles (reflecting the loss of $\sigma 1$, $\mu 1$, and $\sigma 3$; Table I) (Fig. 4 *D*). The external radius of the core varies from a maximum of 400 Å for the prominent, turretlike spikes surrounding the fivefold vertices to a minimum of 305 Å at the threefold axes. The 12 turrets have a maximum outer diameter of 184 Å and a 125-Å-deep axial cavity that is 84-Å wide at the top and 51-Å wide at the bottom. The solid T1L-C shell at a radius of ~275 Å also has 150 ellipsoidal nodules. These 30-Å high nodules are arranged in three distinct environments: 60 are located near the 20 threefold axes, 60 are near the 12 turrets, and 30 are directly on the icosahedral twofold axes. The nodules associated with the two- and threefold axes are very similar in shape (~39 by 60 Å), whereas those near the turrets are narrower and longer (~31 by 67 Å). The threefold related nodules appear to make no contacts with each other or their neighbors above the floor of the core surface. However, each nodule on a twofold axis interacts with two neighboring, fivefold-related nodules, and each fivefold-related nodule also appears to make contact with the turret. The morphology of the turret is strikingly different from that of the flower features seen at the fivefold axes in the T1L-V and T1L-I particles (Fig. 4, *B* and *C*).

Internal Features of Reovirus Particles

Radial Density Distributions. Plots of the spherically-averaged density as a function of radius for all three reconstructions reveal the multilayered nature of reovirus (Fig. 5 *A*). The density plots were scaled to the same magnification by assuming that the peak density in the core capsid (radius = 270 Å) was invariant in all viral particles. Large differences in density at radii >300 Å presumably reflect structural changes due to protein losses and conformational changes. Radii <~230 Å correspond to the location of the RNA (Harvey et al., 1981) and display a mean density intermediate between solvent (radius >450 Å) and closely packed protein in the core capsid (radius = 270 Å). Coarse fluctuations in density at radii <240 Å may arise from nucleic acid

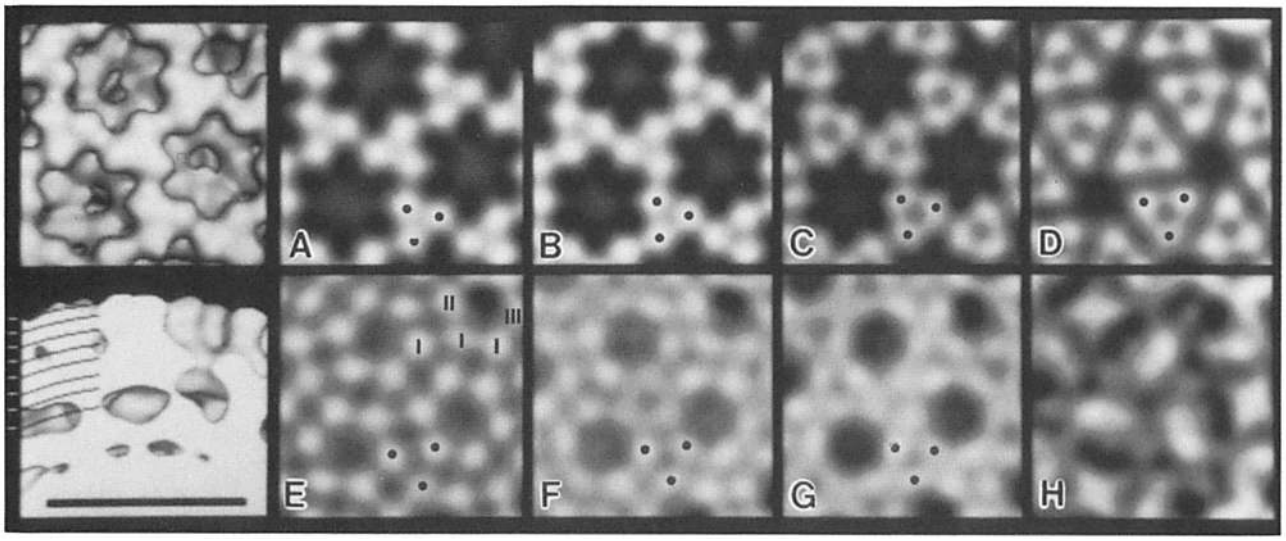

Figure 8. Close-up surface-shaded and projected density views of the TIL-I map. The map is viewed down a threefold symmetry axis (*top left*) and from the side (*bottom left*; threefold axis in the center of the section and oriented vertically). Corresponding views at decreasing radii are indicated by the tick marks and arcs in the side view (*bottom left*). Three classes of $\mu 1$ subunits are identified at lower radii as I-III (*E*). Dots in *A–G* identify the subunits in one trimer and trace the rotation ascribed to $\mu 1$. *A–H*, respectively, correspond to radii of 390, 378, 365, 353, 340, 323, 315, and 303 Å. Bar, 200 Å.

packing. More likely, these fluctuations are a consequence of Fourier series termination errors due to the finite resolution of the maps (Yeager, 1975) and of enforcing icosahedral symmetry. The number of points used to calculate each radial density plot, and hence the error, is inversely proportional to the radius. This may also account for some of the observed increase in density fluctuations at the lowest radii (<150 Å).

Correlation coefficients computed for corresponding density points for the three possible pairwise comparisons of reconstructions provide a quantitative assessment of the variance of structural features as a function of radius (Fig. 5 *B*). All three reconstructions appear to have similar density distributions for radii between 250 and 320 Å. TIL-V and TIL-I (V vs. I, Fig. 5 *B*) additionally show strong correlations for features between radii of 320 and 360 Å. These correlations are maximal only when the data have been scaled to the same magnification as described above, thereby validating the scaling procedure that was used. The nearly zero correlation for densities beyond a radius of 420 Å is expected for predominantly solvent regions outside the particle boundaries. Fluctuating correlations for densities at radii <150 Å presumably reflect systematic errors and noise in the data as described above.

Density Projections at Defined Radii. Spherically averaged density plots (Fig. 5 *A*) provide a simplified view of the distribution of mass in the TIL-V, TIL-I, and TIL-C reconstructions. The corresponding projected mass density at defined radii for these structures (Fig. 6) displays the complex internal architecture of reovirus and allows structural comparisons of the three particles.

Between radii of 270 and 300 Å (e.g., Fig. 6, *E* and *F*) the structures appear nearly identical. This suggests that the location and composition of the proteins corresponding to the inner radii of TIL-C are the same in these particles. The close correspondence of the maps in this region confirms the validity of the density scaling (Fig. 5 *A*) and provides a compelling basis for correlating the observed densities with known reovirus proteins (see Discussion). The density maps from radii of 335 to 360 Å are also nearly identical for TIL-V and TIL-I (Fig. 6, *C* and *D*). The TIL-C map is markedly different at a radius of 335 Å due to the absence of the outer capsid proteins and to the relatively high contrast of the core spike. The high contrast at a radius of 335 Å occurs because the surface of TIL-C is exposed to solvent, whose density differs markedly from protein, whereas the densities in TIL-V and TIL-I at this radius are internal (i.e., less exposed to solvent). The distinctive five-pointed, flowerlike structures centered on the fivefold axes in the surface-shaded maps of TIL-V and TIL-I (Figs. 4 and 6, *top row*) come into view at a radius of ~360 Å (Fig. 6 *C*). Notably, the flowers have petals with a left-handed skew and appear to form a central cap of density (~25-Å thick) over the fivefold centered channel evident at lower radii.

The most distinctive features of the surface view of TIL-C are the surface spikes, or turrets, centered on the fivefold axes (Figs. 4 and 6, *top row right*). In contrast to TIL-V and TIL-I, TIL-C has no cap to close the fivefold cavity (Fig. 6 *C*). The outer circumference of the spike density in TIL-C has the same morphology and position as the pointed ends of the petals in the TIL-V and TIL-I maps (radius ~360 Å; Fig. 6 *C*). At a radius of 390 Å (Fig. 6 *B*), the tips of the TIL-C turrets are visible, whereas the TIL-V and TIL-I maps display no density in the corresponding regions at this radius. This implies that a major structural rearrangement has taken place in the mass around the fivefold axes in TIL-C, compared with TIL-V and TIL-I. At a radius of 390 Å TIL-V and TIL-I are also distinct, presumably reflecting the different capsid compositions and also differences in contrast due to solvent accessibility. Only TIL-V displays density at a radius of 415 Å, which exceeds the maximum radii of TIL-I and TIL-C (Fig. 6 *A*). Interestingly, the orientation of the

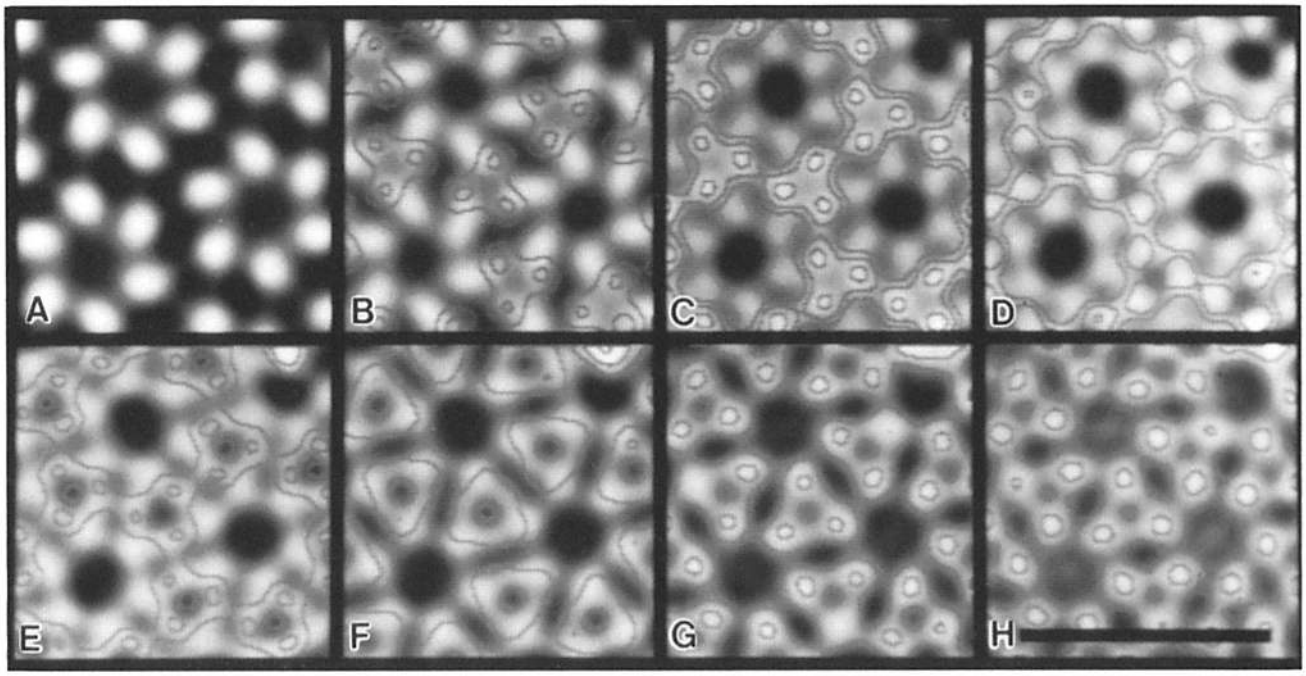

Figure 9. Close-up projected density maps of T1L-V overlaid with corresponding contoured maps of T1L-I, centered down a threefold symmetry axis. *A–H*, respectively, correspond to radii of 405, 394, 384, 373, 365, 357, 349, and 340 Å. Bar, 200 Å.

hexameric features in T1L-V at high radius (415-Å radius, Fig. 6 *A*) is nearly identical to that at low radius (335-Å radius, Fig. 6 *D*).

Discussion

The following interpretations of the density maps of the three particle forms of reovirus strain T1L are organized according to the component proteins. Particular attention is given to protein locations and stoichiometries, protein–protein interactions, and protein conformational changes. Suggestions are made regarding the implication of various structural features to the functional properties of virion (T1L-V), ISVP (T1L-I), and core (T1L-C) particles.

Protein σ3 (41 kD): Difference Map between Virion and ISVP

The changes that occur during the proteolytic conversion of virions to ISVPs include: (*a*) degradative cleavage and loss of protein σ3; (*b*) additional proteolytic cleavage of protein μ1/μ1C to yield cleavage products which remain as components of ISVPs (Nibert and Fields, 1992); and (*c*) conformational change of protein σ1 from a compact to a more extended form (Furlong et al., 1988). Of these changes, the loss of σ3 should account for nearly all the difference in mass between ISVPs and virions. A difference map computed by subtracting the reconstruction of T1L-I from that of T1L-V (Fig. 7) should therefore primarily reveal the σ3 density. This difference map displays 600 morphological subunits, grouped in either hexameric or tetrameric clusters as described for T1L-V (see Results; Fig. 4). A complete hexameric cluster is centered around solvent channels at each of the 60 P3 lattice positions; in contrast, a tetrameric cluster, arranged as a partial hexamer with two subunits missing from one side, is centered at each of the 60 P2 positions (Fig. 7, *B* and *C*). The subunits are ellipsoidal and correspond to the fingerlike features that project from the surface of intact virions (see Results; Metcalf et al., 1991). We suggest that each subunit represents a σ3 monomer, implying that a total of 600 copies of σ3 are present in the outer capsid of reovirus. The volume determined for the total density in the difference map was found to be only slightly greater (~1%) than the estimated volume occupied by 600 copies of σ3 (assuming a mass of 41 kD and density of 1.30 g/cm³), consistent with our interpretation of these features.

Each of the putative ellipsoidal σ3 subunits has a diameter of ~36 Å and a long axis of ~67 Å, spanning radii from 360 to 427 Å in the outer capsid, as seen in the side view of the difference map (Fig. 7, *E* and *F*). Notable in this section is a slight bend in each subunit at a radius of 395 Å, suggesting that σ3 may have a hinged, two-domain tertiary structure. In the side view it is also apparent that at no radii do σ3 subunits from adjacent hexameric clusters interact, suggesting that σ3 does not independently form an icosahedral lattice structure. Scattered regions of density, well above the noise level but not accounted for by σ3 (arrows in Fig. 7, *B* and *E*; open regions surrounding the P1 positions, Fig. 7, *B* and *C*), may be contributed by proteins μ1, λ2, or σ1.

Protein μ1 (76 kD): Complex, Interlocking Structure in the Outer Capsid

The μ1 protein is the other major component of the outer capsid of reovirus virions. Although most μ1 is present in proteolytically cleaved forms in both virions and ISVPs, most of its mass remains associated with these particles as cleavage products (Nibert et al., 1991*b*; Nibert and Fields, 1992). The T1L-I reconstruction (Fig. 4 *C*) displays 200 features surrounding the P2 and P3 channels in the outer capsid which appear trimeric at radii >353 Å (Fig. 8, *A–D*). At lower radii (340–323 Å; Fig. 8, *E* and *F*), the subunits of

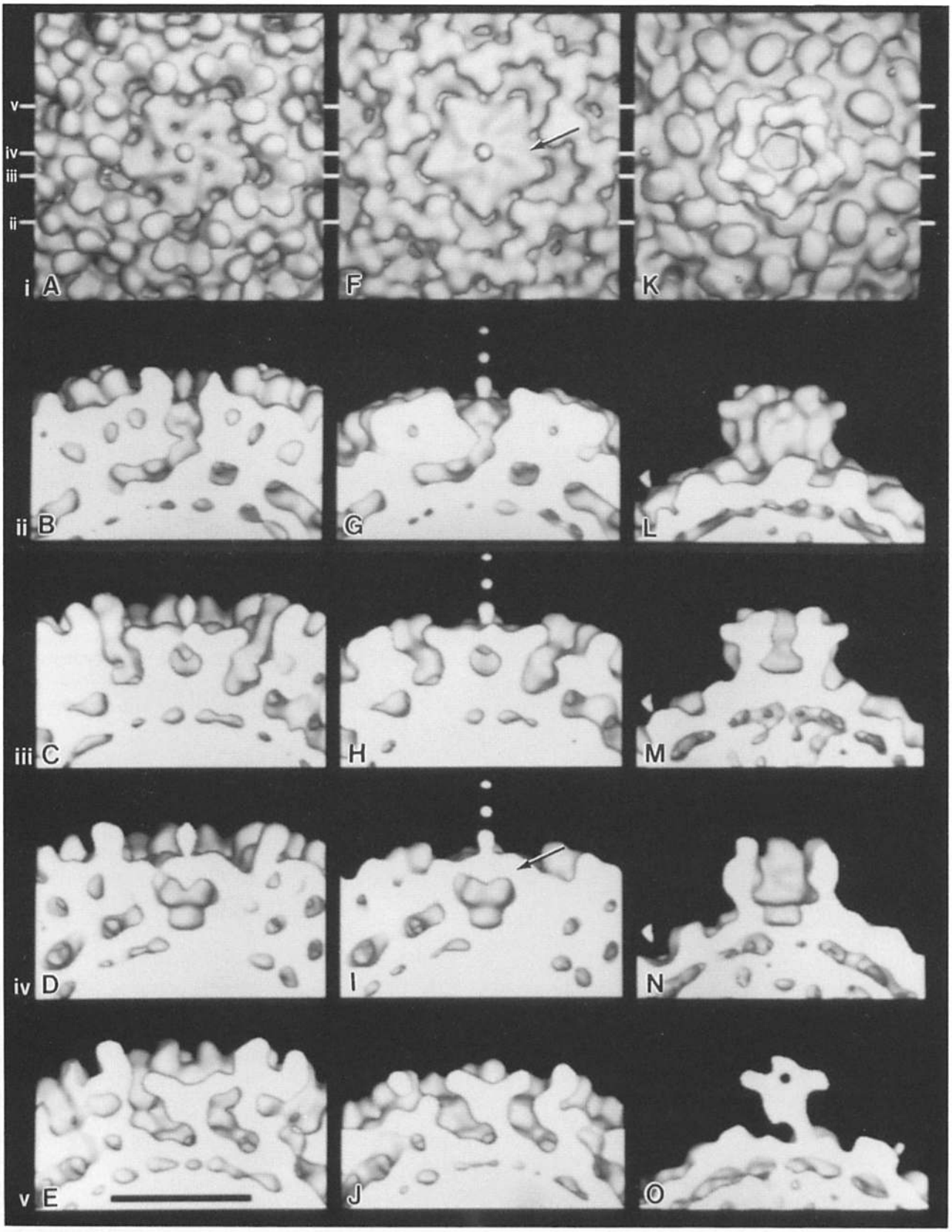

Figure 10. Close-up surface-shaded views down a fivefold axis of TlL-V (*left column*), TlL-I (*middle column*), and TlL-C (*right column*). The tick marks in the top panels (*A*, *F*, and *K*, row *i*) identify the locations of cross-sectional views displayed in rows *ii–v*. For instance, the topmost tick marks correspond to the side views in row *v*. The bottommost tick marks correspond to the side views in row *ii*. Arrows in *F* and *I* identify the putative hinge region of λ2. Bar, 200 Å.

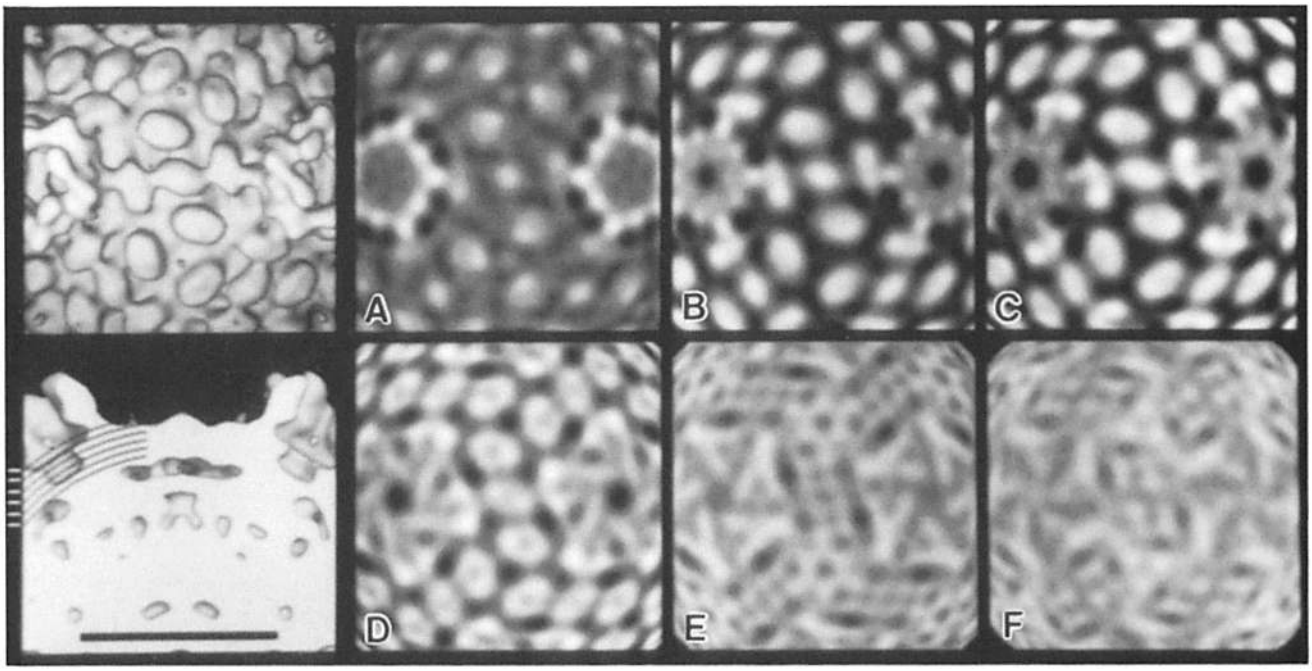

Figure 11. Close-up surface-shaded (*left column*) and projected density views (*A–F*) of the TIL-C map. All views (except *bottom left*) are along a twofold symmetry axis. The side view (*bottom left*) displays arcs and tick marks corresponding to the projection density maps displayed in *A* to *F* at respective radii of 311, 300, 290, 280, 270, and 260 Å. Bar, 200 Å.

each trimer are organized in hexameric and tetrameric clusters similar to and in near radial register with the σ3 clusters, at higher radii in TIL-V (~415 Å). Each subunit, proposed to represent a single copy of μ1, has a diameter of ~28 Å and a rodlike morphology spanning radii from 306 to 395 Å in the outer capsid of both TIL-V and TIL-I. These features are completely absent from the density map of cores, consistent with the absence of protein μ1 in TIL-C. Thus, these results suggest that 600 copies of μ1 are present in virions and ISVPs, equal to the copy number of σ3 in virions as previously suggested by biochemical analysis (Jayasuriya et al., 1988).

The path of the putative μ1 subunits at decreasing radii in the outer capsid is more complex than that of σ3. The center of the rodlike subunit is directed radially down to 365 Å (Fig. 8, *A–C*). The rod then abruptly bends in an azimuthal direction such that its path between 365 and 353 Å corresponds to an ~40° counterclockwise rotation of the trimeric unit (Fig. 8, *C* and *D*). Between 353 and 340 Å, the μ1 subunits splay away from the local and strict threefold axes (Fig. 8, *D* and *E*). Between 340 and 315 Å, they again bend azimuthally to generate an ~20° clockwise rotation of the original trimers (Fig. 8, *E–G*).

The complex path of μ1 leads to a variety of contacts between neighboring subunits at different radii, which may be important for the role of μ1 in forming and stabilizing the outer capsid. Intratrimeric contacts are present over the entire length of μ1, but appear strongest at highest radii (>390 Å; Fig. 8 *A*). In addition, from 390 to 365 Å (Fig. 8, *A–C*), most μ1 subunits also make contact with a single μ1 subunit from an adjacent trimeric unit, which links the trimers across the surface of TIL-I. Intertrimer contacts are notably absent at a radius of 353 Å (Fig. 8 *D*) as the μ1 density shifts. From 340 to 315 Å (Fig. 8, *E–G*), three classes of individual μ1 subunits are distinguished by their interactions with neighboring subunits. There are 60 P3 hexamers centered around channels at the 20 strict threefold axes, accounting for 360 of the 600 μ1 subunits. All these subunits, designated class I, appear to make nonidentical contacts with four adjacent μ1 subunits (Fig. 8 *E*). The remaining 240 μ1 subunits are centered around the 60 P2 channels. 120 of these make contacts with four neighbors as in class I, 60 make contacts with three adjacent μ1 subunits (class II), and 60 make contacts with only two (class III). The class II and III μ1 subunits also contact the fivefold flowerlike features located at the 12 P1 positions (accounted for by λ 2; see below). The multiple contacts between μ1 subunits at different radii form a complex, interlocking structure.

Intimate Interactions between σ3 and μ1

The formation of stable σ3–μ1 complexes seems to play a significant role in viral morphogenesis (Lee et al., 1981*a*; Tillotson and Shatkin, 1992). Comparisons of TIL-V and TIL-I (Figs. 7–9) display intimate interactions between the subunits of σ3 and μ1, suggesting that these proteins bind in a highly specific fashion. Contacts between σ3 and μ1 may be dominant over those between σ3 subunits within the hexameric and tetrameric clusters seen on the surface of virions. For example, ellipsoidal σ3 subunits begin to contact neighboring σ3 subunits only at radii lower (e.g., 373 Å; Figs. 6 *B* and 9 *D*) than where they already have extensive contacts with neighboring μ1 subunits. This suggests that the icosahedral packing of σ3 is a direct consequence of the underlying organization of μ1.

The arrangement of μ1 subunits looks virtually identical in the TIL-V and TIL-I reconstructions at radii >365 and <349 Å (Fig. 9, *B–E* and *G–H*); however, densities near a

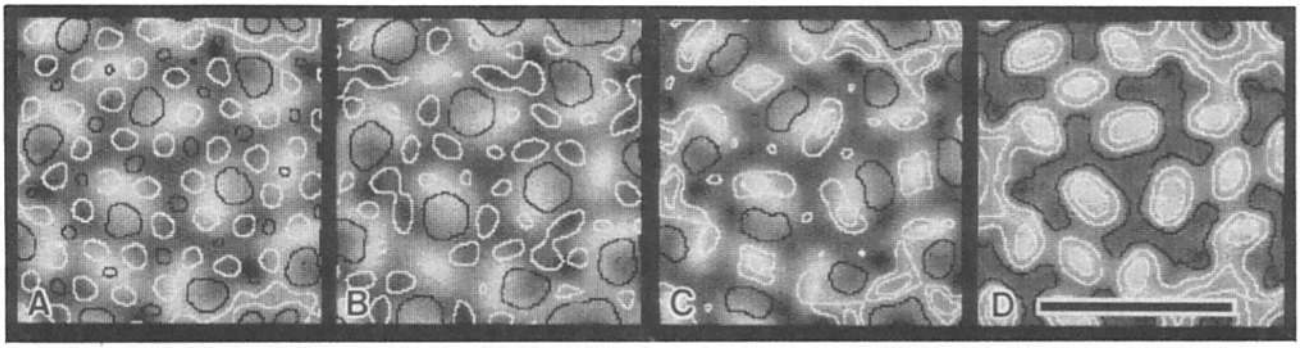

Figure 12. Projected density map of TIL-C (radius = 290 Å) overlaid with contoured maps of TIL-I at radii of 340, 324, 307, and 290 Å (*A–D*, respectively). The TIL-C map representing radius 290 Å was magnified in *A–C* to match the radial values of the TIL-I contours (340, 324, and 307 Å, respectively). White represents highest density (i.e., protein) in the grey scale images and positive density for the contours and black lines define negative density regions. Bar, 200 Å.

radius of 357 Å in these reconstructions do not match as well (Fig. 9 *F*). This section is beneath the proposed minimum radial extent of σ3 so the differences presumably reflect small rearrangements in μ1 as a consequence of σ3–μ1 interactions in TIL-V. The contacts between μ1 subunits appear to be weak or absent at a radius of 353Å (Fig. 8 *D*). This may provide μ1 with sufficient flexibility to assume slightly different conformations in the presence and absence of σ3. Also, each σ3 subunit appears to contact primarily one μ1 subunit at higher radii (394–384 Å; Fig. 9, *B* and *C*) but appears sandwiched between two μ1 subunits at lower radii (373–365 Å; Fig. 9, *D* and *E*). Slight changes in conformation of μ1 and interlocking of an external region of μ1 subunits by σ3 may have relevance for the relative stabilities of virions and ISVPs (Nibert et al., 1991*a*).

Protein λ2 (144 kD): Large Conformational Change between ISVP and Core

λ2 has been ascribed to the core spikes, or turrets, protruding from the surface of TIL-C (White and Zweerink, 1976; Fig. 4 *D*), consistent with isolated spikes comprising pentameric oligomers of λ2 molecules (Ralph et al., 1980). Epitopes on λ2 are also accessible for antibody labeling on both virions and ISVPs (Hayes et al., 1981; Virgin et al., 1991). The flower-shaped surface features in TIL-V and TIL-I (Fig. 10, *A* and *F*) presumably correspond to these exposed domains of λ2. Protein σ1 is assigned to the small density centered on the fivefold axis and radially projecting from the pentameric features in TIL-V and TIL-I (Fig. 10, *B* and *G*) as discussed below. The difference between the flower-shaped feature in TIL-V and TIL-I and the turret in TIL-C is attributed to a dramatic conformational change of λ2 during the transition from ISVPs to cores. The columnar regions of the spike, spanning radii of ~305–370 Å, are very similar in all three maps but blend with densities attributable to σ3 and μ1 in TIL-V and TIL-I. In virions and ISVPs, part of the putative λ2 pentamer forms a five-pointed flower by capping the spike with petallike densities that have one end at a point, or tip, and the other reaching towards the fivefold axis (Fig. 10, *A* and *F*). The five points remain in the same location for all three maps, and the distance between neighboring points is 184 Å. In the transition from TIL-I to TIL-C, the petals appear to be released at the center, and the freed ends move ~30 Å outward and upward to rotate ~25° clockwise (Figs. 10, rows *i* and *iv*; and 6 *B*) around a hinge (arrow in Fig. 10, *F* and *I*). This striking conformational change in the outer domain of the λ2 subunits exposes an 84-Å-wide central cavity (Fig. 10, *K* and *N*) and extends the spikes to a particle radius of 400 Å in TIL-C (Fig. 10 *M*).

Protein λ2 is an essential component of the transcriptase apparatus in reovirus cores (White and Zweerink, 1976) and manifests the guanylyltransferase activity required for adding a 5′ cap to the nascently transcribed viral mRNAs (Cleveland et al., 1986; Seliger et al., 1992). In addition, the viral mRNAs are thought to exit transcribing cores through the channels of the λ2 spikes (Bartlett et al., 1974). The large conformational change in λ2 between ISVPs and cores supports the latter hypothesis and thus may be critical for transcriptase activity.

λ2 Interacts with Other Proteins in the Core and Outer Capsids

Structural details of the spikes indicate that λ2 is best considered an outer capsid protein that resists proteolysis and remains as a component of core particles. Calculation of the solvent-excluded volume in the TIL-C turret predicts that λ2 primarily forms that portion of the turret extending above the main core shell. Sixty copies of a 144-kD protein should occupy a volume of 11.2×10^6 Å^3 (assuming a protein density of 1.30 g/cm^3). This compares with a volume of 11.5×10^6 Å^3 for the density in TIL-C at radii >305 Å, which is just above the core surface nodules (Fig. 11, *A* and *B*). This radial value is consistent with the size of alkali-treated core particles which lose their spikes but retain a full genome (White and Zweerink, 1976; Harvey et al., 1981). Densities at the base of each turret (radii ~290–311 Å) alternate about the fivefold axis with other densities (Fig. 11, *A–C*) that appear continuous with adjacent nodules and with Y-shaped structures beneath the turret base (Fig. 11 *E*). These Y-shaped densities may represent core protein λ1, with which λ2 interacts via a small region at the base of each turret (see below).

Each of the three outer capsid proteins (σ3, μ1, σ1) of reovirus makes contact with λ2. The λ2 petals appear to contact the σ1 fiber on the fivefold axis in virions and ISVPs (described in detail below), consistent with antibody binding studies that indicate close proximity of σ1 and λ2 proteins (Lee et al., 1981*a*; Virgin et al., 1991). The interaction between λ2 pentamers and σ1 oligomers (either trimeric or tetrameric) may necessitate a symmetry mismatch as occurs in the head-to-tail junctions in double-stranded DNA bacte-

riophages (Hendrix, 1978). In virions, one subunit of σ3 (at position b in Fig. 4 *A*) from each P2 tetramer contacts the tip of a λ2 petal at a radius of ~367 Å (Fig. 10 *A*). This λ2-σ3 interaction may modify the conformation of the λ2 petals to cause the slight difference in appearance of the λ2 flower observed between virions and ISVPs (Fig. 10 *A*). Each λ2 subunit is also embraced by one class II and one class III μ1 subunit over a span of ~10 Å (radii 335–325 Å) in T1L-I (Fig. 10, *F* and *I*). The portion of λ2 contacted by μ1 appears to be near the hinge around which λ2 bends (Fig. 10 *I*). Thus, these contacts between λ2 and μ1 may be important for maintaining the λ2 pentamer in the flower-shaped conformation seen in virions and ISVPs, and changes in these contacts may facilitate the ISVP-to-core transition.

Protein σ1 (51 kD): Conformational Change between Virion and ISVP

Images of negatively stained reovirus protein σ1, the viral receptor–recognition protein, display a fiber >400 Å in length with a 20–40-Å-diam tail and an ~80-Å-diam globular head (Furlong et al., 1988; Banerjea et al., 1988). These studies also suggest that σ1 can assume at least two distinct conformations in particles: the extended one and a poorly characterized, more compact form. Negative stain EM indicates that σ1 commonly assumes the more compact form in virions of most reovirus strains, but extends dramatically from the particle surface in ISVPs (Furlong et al., 1988). Extension of σ1 presumably facilitates binding to cell-surface receptors. The amino-terminal tail of σ1 is anchored in the virion capsid, and a small NH_2-terminal sequence of less than 121 residues is sufficient to direct the assembly of σ1 into virions (Nibert et al., 1990; Mah et al., 1990). In addition, an oligomeric form of σ1 is necessary for binding to cellular receptors (Duncan et al., 1991), but the exact quaternary arrangement of σ1 has been debated. Current evidence suggests that σ1 probably occurs in viral particles as a trimer (Strong et al., 1991) or tetramer (Fraser et al., 1990).

Images of T1L-I (Fig. 1, *B* and *D*) and some T1L-V (Fig. 1 *A*) clearly reveal the presence of long, extended fibers that we identify as σ1. A higher fraction of T1L-I versus T1L-V particles adopt a preferred orientation in vitrified specimens (Fig. 1, *A*, *B*, and *D*). Perhaps the extended σ1 fibers interact with the air-water interface to orient the particles. No fibers were detected in images of T1L-C particles (Fig. 1 *C*), consistent with the absence of σ1 in cores (Table I). Surface-shaded views down the fivefold axes of T1L-V and T1L-I (Fig. 10, *A* and *F*) show density emerging radially from the center of the λ2 flower that we attribute to σ1. In T1L-V, this density is knoblike, ~30 Å in diameter, and extends only ~46 Å above the flower (Fig. 10 *C*). In T1L-I, discontinuous, beaded densities extend radially ~110 Å above the flower (Fig. 10 *H*). These discontinuous densities become connected if the density map is corrected for effects of the microscope contrast transfer function (data not shown). The density has a diameter of ~22 Å and resembles a fiber. σ1 fibers often appear bent in micrographs, which presumably accounts for the absence of a complete fiber in the icosahedrally averaged reconstructions. Also, the averaging procedures used in our analysis and the limited resolution of the density maps preclude determination of the oligomeric state of σ1. The base of the fiber appears to merge with the 25-Å-thick cap formed by the apparently mobile outer domain of each λ2 subunit, and it appears to extend through and slightly below the cap into the large fivefold cavity (Fig. 10, *D* and *I*). If indeed σ1 lies in a unique folded conformation on the surface of virions, it is not observed in the symmetry-averaged maps. Since σ1 mediates the capacity of virions to agglutinate red blood cells (Burstin et al., 1982; Dermody et al., 1990), it must be accessible on the surface of T1L-V. The morphological switch from a short and knob-like feature in T1L-V to a longer and thinner feature in T1L-I strongly suggests at least two separate (compact and extended) conformations of σ1.

Other Core Proteins: λ1 (137 kD), σ2 (47 kD), λ3 (142 kD), and μ2 (83 kD)

The T1L-C reconstruction at radii primarily below the level of the λ2 spikes (Fig. 11) reveals different types of symmetry-related surface nodules (Fig. 11, *top left*, *A–C*) and Y-shaped structures surrounding the fivefold axes (Fig. 11, *D–F*). These features are also observed in T1L-V and T1L-I (Fig. 6 *E*). Unfortunately, the icosahedral organization of proteins in the core capsid is not readily evident.

Removal of λ2 from cores renders λ1 more susceptible to iodination (White and Zweerink, 1976), suggesting that λ2 and λ1 may interact near the icosahedral vertices. In the T1L-C map, ten distinct densities are arranged around the base of the turret. Every other density contacts a fivefold-related surface nodule (Fig. 11 *B*). At radii beneath the turret (~280–260 Å; Fig. 11, *D–F*), there are five Y-shaped structures, which appear continuous with the fivefold-related nodules at higher radii. We suggest that these nodules and Y-shaped densities may consist primarily of protein λ1, and may possibly represent λ1 dimers since there are ~120 λ1 molecules in each virion.

The σ2 protein has been proposed to occupy a more internal position than λ1 in the core capsid (White and Zweerink, 1976). Because λ1 and σ2 both bind dsRNA (Schiff et al., 1988; Huismans and Joklik, 1976), they are likely to reside near the inner surface of the core shell. Recent estimates for the number of σ2 molecules in viral particles range between 120 and 180 (Coombs et al., 1990; Schiff et al., 1988). Thus, σ2 may also contribute to some of the 150 nodules on the core surface, in which case, both λ1 and σ2 may span the core capsid. λ1 and σ2 should account for the bulk of the core shell (Table I). In fact, measurements of the solvent-excluded volume of this shell in T1L-V, T1L-I, and T1L-C (29.7, 30.6, and 31.8 × 10^6 $Å^3$, respectively) are quite close to the estimated volume (29.2 to 32.8 10^6 $Å^3$) of 120 copies of λ1 (137 kD) and 120 to 180 copies of σ2 (47 kD) per virion, using an average protein density of 1.30 g/cm^3. Inclusion of the minor core proteins, λ3 and μ2, does not significantly alter these calculations. The current estimate of ~12 molecules each of λ3 and μ2 per particle (Table I) suggests that they may lie near the 12 icosahedral vertices inside the capsid.

Interactions between the Core Capsid and μ1

To examine interactions between the outer capsid and core, contour maps of the T1L-I map for radii between 340 and 290 Å were superimposed on the projected grey-level map of the T1L-C reconstruction for densities at a radius of

290 Å, which displays the 150 TIL-C surface nodules (Fig. 12). At 340-Å radius, well above the core surface, contours of the TIL-I map show the hexameric arrangement of μ1 subunits (Fig. 12 *A*). At 324-Å radius, contours in the TIL-I map are again ascribed to μ1, but a regular lattice arrangement is less apparent (Fig. 12 *B*). Some contact between μ1 and the core nodules is evident near a radius of 307 Å (Fig. 12 *C*). At a radius beneath the minimum radial extent of μ1 (290 Å; Fig. 12 *D*), there is close correspondence between the TIL-I contours and the TIL-C density. This indicates that the core nodules in TIL-I are in the same location as in TIL-C.

The sharp transition from μ1 to core nodules suggests a substantially smaller area of contact between μ1 and the core than that observed between μ1 and σ3 in the outer capsid. This solvent-accessible space between the outer capsid and the TIL-C surface, separated by the nodules, may account for the lucent ring seen in images of TIL-V and TIL-I particles (Fig. 1, *A* and *B*). Also, the lattice formed by 600 copies of μ1 does not appear to align directly with an icosahedral arrangement of the 150 core nodules, so μ1 may interact somewhat differently with each of the different nodules. Our interpretation suggests only weak interactions between μ1 and the core nodules and thus that the arrangement of the core shell may have little, if any, influence in directing the assembly of μ1 or in maintaining precise contact between the capsid shells. Specific interactions between μ1 (subunit classes II and III) and λ2 at the fivefold axes as described above may be more important in nucleating the assembly of μ1 subunits into an icosahedral lattice.

Liquid Crystalline Packing of the Genomic dsRNA

The genome of mammalian reoviruses consists of ten unique segments of dsRNA with a total mass of 15.1 megadaltons. Low-angle x-ray scattering suggested that the dsRNA is closely packed with an average separation of 26 Å between dsRNA helices (Harvey et al., 1981). Close-to-focus images of frozen-hydrated cores (Fig. 1 *E*) reveal a pattern of striations that resemble fingerprints. We ascribe these features to parallel strands of genomic dsRNA in the core interior. These striations exhibit a spacing of 25 to 27 Å, consistent with measurements of Harvey et al. (1981). Similar striations in images of Herpes Simplex virus type 1 (Booy et al., 1991) and bacteriophages T4 and λ (Lepault and Leonard, 1985; Lepault et al., 1987) have been attributed to closely packed strands of dsDNA comprising the genomes of those viruses. Thus, the genomic dsRNA of reoviruses might be packed within the core shell as nematic liquid crystals with neighboring dsRNA strands packed in parallel (Lepault et al., 1987). How this arrangement accommodates or affects the movement of dsRNA strands within transcriptionally active particles remains to be defined.

Conclusions

Three structural forms of type 1 Lang reovirus (virions [TIL-V], intermediate subviral particles [TIL-I], and cores [TIL-C]) have been examined by cryoEM and image reconstruction. The size and complexity of reovirus particles has so far thwarted examination at atomic resolution by x-ray crystallography (Coombs et al., 1990). Our reconstructions at moderate resolution (27–32 Å) provide important structural data for addressing key questions regarding viral function. Analysis of the three-dimensional maps and known biochemical composition allows determination of capsid protein location, globular shape, stoichiometry, quaternary organization, and interactions with adjacent capsid proteins. The three particle forms of reoviruses provide "snapshot" views of the virus at discrete, early stages of infection. Comparisons of the virion, ISVP and core structures and examination of difference maps reveal dramatic changes in supramolecular structure and protein conformation that are related to the early steps of reovirus infection. In general, the reovirus structure and that of other members of the *Reoviridae*, such as rotavirus (Yeager et al., 1990) or bluetongue virus (Hewatt et al., 1992) are more dissimilar than similar, except for their overall size and the T = 13*l* arrangement of the outer capsid proteins. The segmented dsRNA genome of reovirus resides at radii <240 Å and appears to be packed in a liquid crystalline fashion that is analogous to the packing of dsDNA in Herpes Simplex virus type 1 and bacteriophages T4 and λ.

The intact virion (~850-Å diam) is designed for environmental stability in which the dsRNA genome is protected not only by tight σ3-μ1, λ2-σ3, and λ2-μ1 interactions in the outer capsid but also by a densely packed core shell formed primarily by λ1 and σ2. The major outer capsid proteins are σ3 and μ1. The virion surface displays 60 tetrameric and 60 hexameric clusters of fingerlike subunits. Based on difference maps between the virion and ISVP, we have conclusively identified these subunits as σ3, as suggested by Metcalf et al. (1991). The ellipsoidal σ3 subunits span radii from 360–427 Å with a slight kink at 395 Å, suggesting a two domain structure. The remaining outer capsid layer is formed by 200 trimers of rod-shaped μ1 subunits that span radii from 306–395 Å.

Depending on the circumstances of viral infection, virions undergo cleavage by enteric or endosomal/lysosomal proteases, to generate the activated ISVP (~800-Å-diam). This transition involves the release of the 600 σ3 subunits. In addition, there is a striking change in the vertex-associated cell attachment protein σ1 from a poorly visualized, more compact form, to an extended, flexible fiber. Although we cannot resolve the entire σ1 molecule or discern its quaternary structure, the density we attribute to this protein is very distinct from the domains of λ2 that enclose the spike cavity in virions and ISVPs, attributed to σ1 by Metcalf et al. (1991). The possible symmetry mismatch between the trimeric or tetrameric σ1 fibers and the pentameric flower-shaped vertex structures (λ2) may faciliate rotation at the base of σ1. Several features of σ1 suggest that it is extremely well designed to maximize interactions with cell surface receptors: (*a*) the extended conformation of the 12 fibers; (*b*) the flexibility of the fiber; and (*c*) the potential for rotation at the fiber base.

Transcription of viral mRNAs is mediated by the core particle (~600-Å diam), generated from the ISVP after penetration and uncoating. The transition from ISVP to core involves release of the 12 σ1 fibers and the 600 μ1 subunits. The surface of the core displays 150 nodules that merge with a solid shell centered at a radius of ~275 Å. We suspect that the knobs and shell consist primarily of λ1 and σ2, which account for >90% of the core mass. In the virion and ISVP, flower-shaped pentamers of λ2 are centered at the vertices. In the ISVP-to-core transition, domains of the λ2 subunits

rotate upward and outward to form a turretlike structure extending from radii 305–400 Å, with an outer diameter of 184 Å, and a central channel 84-Å wide. This conformational change allows the potential diffusion of substrates for transcription and exit of newly synthesized mRNA segments.

The virion, ISVP and core density maps reveal novel features of the inter-particle transitions relevant to understanding early steps in the reovirus replication cycle. These transitions are characterized by protein degradation and disassembly. The loss of $\sigma 3$ may trigger the transition of $\sigma 1$ from a compact to an extended conformation. In a similar fashion, the release of $\mu 1$ and $\sigma 1$ may trigger the transition of $\lambda 2$ from a closed flowerlike pentamer to an open turretlike structure. These speculations are based on the interpretation of the density maps and provide a foundation for future experiments. In summary, the essence of these orchestrated events is that reovirus is superbly designed to undergo stages of controlled disassembly in which the release of oligomeric protein layers in the outer capsid is coordinated with large protein conformational changes at the icosahedral vertices, important sites for virus–cell interactions and viral transcription.

We gratefully acknowledge R. H. Cheng for providing programs to help analyze particle images using cross-correlation techniques and to help estimate the effects of the microscope contrast transfer function on the three-dimensional reconstructions and D. M. Belnap for aid in calibrating the micrograph magnifications.

This research was supported by National Institutes of Health grants GM33050 (T. S. Baker), AI31535 (M. Yeager), and 5R37 AI13178 (B. N. Fields); a Grant-in-Aid from the American Heart Association, National Center and a grant from the Gustavus and Louise Pfeiffer Research Foundation (M. Yeager); a program project grant 2P50NS16998 from the National Institute of Neurological and Communicative Disorders and Stroke and a grant from the Shipley Institute of Medicine (B. N. Fields); a NIH research service award 5T32 HLO7627 (M. L. Nibert); and a grant from the Lucille P. Markey Trust for support of the Purdue Structural Biology program. M. Yeager is an Established Investigator of the American Heart Association.

Received for publication 22 January 1993 and in revised form 27 April 1993.

References

Adrian, M., J. Dubochet, J. Lepault, and A. W. McDowall. 1984. Cryo-electron microscopy of viruses. *Nature (Lond.).* 308:32–36.

Aldroubi, A., B. L. Trus, M. Unser, F. P. Booy, and A. C. Steven. 1992. Magnification mismatches between micrographs: corrective procedures and implications for structural analysis. *Ultramicroscopy.* 46:175–188.

Baker, T. S. 1992. Cryo-electron microscopy and three-dimensional image reconstruction of icosahedral viruses. Proc. 10th Eur. Congress Electron Microsc. Granada, Spain. 3:275–279.

Baker, T. S., J. Drak, and M. Bina. 1988. Reconstruction of the three-dimensional structure of simian virus 40 and visualization of the chromatin core. *Proc. Natl. Acad. Sci. USA.* 85:422–426.

Baker, T. S., W. W. Newcomb, F. P. Booy, J. C. Brown, and A. C. Steven. 1990. Three-dimensional structures of maturable and abortive capsids of equine herpesvirus 1 from cryoelectron microscopy. *J. Virol.* 64:563–573.

Baker, T. S., W. W. Newcomb, N. H. Olson, L. M. Cowsert, C. Olson, and J. C. Brown. 1991. Structures of bovine and human papillomaviruses: analysis by cryoelectron microscopy and three-dimensional image reconstruction. *Biophys. J.* 60:1445–1456.

Banerjea, A. C., K. A. Brechling, C. A. Ray, H. Erickson, D. J. Pickup, and W. K. Joklik. 1988. High-level synthesis of biologically active reovirus protein $\sigma 1$ in a mammalian expression vector system. *Virology.* 167:601–612.

Bartlett, N. M., S. C. Gillies, S. Bullivant, and A. R. Bellamy. 1974. Electron microscopy study of reovirus reaction cores. *J. Virol.* 14:315–326.

Belnap, D. M., W. D. Grochulski, N. H. Olson, and T. S. Baker. 1993. Use of radial density plots to calibrate image magnification for frozen-hydrated specimens. *Ultramicrosc.* 48:347–358.

Bodkin, D. K., and B. N. Fields. 1989. Growth and survival of reovirus in intestinal tissue: role of the L2 and S1 genes. *J. Virol.* 63:1188–1193.

Booy, F. P., W. W. Newcomb, B. L. Trus, J. C. Brown, T. S. Baker, and A. C. Steven. 1991. Liquid-crystalline, phage-like packing of encapsidated DNA in Herpes Simplex virus. *Cell.* 64:1007–1015.

Borsa, J., T. P. Copps, M. D. Sargent, D. G. Long, and J. D. Chapman. 1973. New intermediate subviral particles in the in vitro uncoating of reovirus virions by chymotrypsin. *J. Virol.* 11:552–564.

Burstin, S. J., D. R. Spriggs, and B. N. Fields. 1982. Evidence for functional domains on the reovirus type 3 hemagglutinin. *Virology.* 117:146–155.

Carrascosa, J. L., and A. C. Steven. 1978. A procedure for evaluation of significant structural differences between related arrays of protein molecules. *Micron.* 9:199–206.

Caspar, D. L. D., and A. Klug. 1962. Physical principles in the construction of regular viruses. *Cold Spring Harbor Symp. Quant. Biol.* 27:1–24.

Chiu, W. 1986. Electron microscopy of frozen, hydrated biological specimens. *Ann. Rev. Biophys. Biophys. Chem.* 15:237–257.

Cleveland, D. R., H. Zarbl, and S. Millward. 1986. Reovirus guanylyltransferase is L2 gene product lambda 2. *J. Virol.* 60:307–311.

Coombs, K. M., B. N. Fields, and S. C. Harrison. 1990. Crystallization of the reovirus type 3 Dearing core: crystal packing is determined by the $\lambda 2$ protein. *J. Mol. Biol.* 215:1–5.

Crowther, R. A. 1971. Procedures for three-dimensional reconstruction of spherical viruses by Fourier synthesis from electron micrographs. *Philos. Trans. R. Soc. Lond. B. Biol. Sci.* 261:221–230.

Crowther, R. A., D. J. DeRosier, and A. Klug. 1970. The reconstruction of a three-dimensional structure from projections and its applications to electron microscopy. *Proc. Roy. Soc. Lond. A.* 317:319–340.

Dermody, T. S., M. L. Nibert, R. Bassel-Duby, and B. N. Fields. 1990. A $\sigma 1$ region important for hemagglutination by serotype 3 reovirus strains. *J. Virol.* 64:5173–5176.

Dermody, T. S., L. A. Schiff, M. L. Nibert, K. M. Coombs, and B. N. Fields. 1991. The S2 gene nucleotide sequences of prototype strains of the three reovirus serotypes: characterization of reovirus core protein $\sigma 2$. *J. Virol.* 65:5721–5731.

Dubochet, J., M. Adrian, J.-J. Chang, J.-C. Homo, J. Lepault, A. W. McDowall, and P. Schultz. 1988. Cryo-electron microscopy of vitrified specimens. *Quart. Rev. Biophys.* 21:129–228.

Duncan, R., D. Horne, J. E. Strong, G. Leone, R. T. Pon, M. C. Yeung, and P. W. K. Lee. 1991. Conformational and functional analysis of the C-terminal globular head of the reovirus cell-attachment protein. *Virology.* 182:810–819.

Fraser, R. D. B., D. B. Furlong, B. L. Trus, M. L. Nibert, B. N. Fields, and A. C. Steven. 1990. Molecular structure of the cell-attachment protein of reovirus: correlation of computer-processed electron micrographs with sequence-based predictions. *J. Virol.* 64:2990–3000.

Fuller, S. D. 1987. The T=4 envelope of Sindbis virus is organized by interactions with a complementary T=3 capsid. *Cell.* 48:923–934.

Furlong, D. B., M. L. Nibert, and B. N. Fields. 1988. Sigma 1 protein of mammalian reoviruses extends from the surfaces of viral particles. *J. Virol.* 62:246–256.

Furuichi, Y., M. Morgan, S. Muthukrishnan, and A. J. Shatkin. 1975. Reovirus messenger RNA contains a methylated, blocked 5′-terminal structure: $m^7G(5')ppp(5')G^mpCp$-. *Proc. Natl. Acad. Sci. USA.* 72:362–366.

Gomatos, P. J., and I. Tamm. 1963. The secondary structure of reovirus RNA. *Proc. Natl. Acad. Sci. USA.* 49:707–714.

Harvey, J. D., A. R. Bellamy, W. C. Earnshaw, and C. Schutt. 1981. Biophysical studies of reovirus type 3. IV. Low-angle x-ray diffraction studies. *Virology.* 112:240–249.

Hayes, E. C., P. W. K. Lee, S. E. Miller, and W. K. Joklik. 1981. The interaction of a series of hybridoma IgGs with reovirus particles: demonstration that the core protein lambda 2 is exposed on the particle surface. *Virology.* 108: 147–155.

Hendrix, R. W. 1978. Symmetry mismatch and DNA packaging in large bacteriophages. *Proc. Natl. Acad. Sci. USA.* 75:4779–4783.

Hewatt, E. A., T. F. Booth, and P. Roy. 1992. Structure of bluetongue virus particles by cryoelectron microscopy. *J. Struct. Biol.* 109:61–69.

Huismans, H., and W. K. Joklik. 1976. Reovirus-coded polypeptides in infected cells: isolation of two native monomeric polypeptides with affinity for single-stranded and double-stranded RNA, respectively. *Virology.* 70: 411–424.

Jaffe, J. S., and R. Glaeser. 1984. Preparation of frozen-hydrated specimens for high resolution electron microscopy. *Ultramicrosc.* 13:373–378.

Jayasuriya, A. K., M. L. Nibert, and B. N. Fields. 1988. Complete nucleotide sequence of the M2 genome segment of reovirus type 3 Dearing and analysis of its protein product $\mu 1$. *Virology.* 163:591–602.

Joklik, W. K. 1972. Studies on the effect of chymotrypsin on reovirus. *Virology.* 49:700–715.

Joklik, W. 1983. The reovirus particle. *In* The Reoviridae. W. Joklik, editor. Plenum Publishing Corp., New York. 9–78.

Khaustov, V. I., M. B. Korolev, and V. N. Reingold. 1987. The structure of the capsid inner layer of reoviruses. *Arch. Virol.* 93:163–167.

Lee, P. W. K., E. C. Hayes, and W. K. Joklik. 1981*a*. Characterization of anti-reovirus immunoglobins secreted by cloned hybridoma cell lines. *Virology.* 108:134–146.

Lee, P. W. K., E. C. Hayes, and W. K. Joklik. 1981*b*. Protein $\sigma 1$ is the reovirus cell attachment protein. *Virology.* 108:156–163.

Lepault, J., and K. Leonard. 1985. Three-dimensional structure of unstained, frozen-hydrated extended tails of bacteriophage T4. *J. Mol. Biol.* 182: 431–441.

Lepault, J., J. Dubochet, W. Baschong, and E. Kellenberger. 1987. Organization of double-stranded DNA in bacteriophages: a study by cryo-electron microscopy of vitrified samples. *EMBO (Eur. Mol. Biol. Organ.) J.* 6: 1507–1512.

Lucia-Jandris, P. A. 1990. Interactions of mammalian reovirus particles with cell membranes. Ph.D. thesis. Harvard University. Cambridge, MA. 1–178.

Mah, D. C. W., G. Leone, J. M. Jankowski, and P. W. K. Lee. 1990. The N-terminal quarter of reovirus cell attachment protein σ1 possesses intrinsic virion-anchoring function. *Virology.* 179:95–103.

Metcalf, P. 1982. The symmetry of the rovirus outer shell. *J. Ultrastruct. Res.* 78:292–301.

Metcalf, P., M. Cyrklaff, and M. Adrian. 1991. The three-dimensional structure of reovirus obtained by cryo-electron microscopy. *EMBO (Eur. Mol. Biol. Organ.) J.* 10:3129–3136.

Milligan, R. A., A. Brisson, and P. N. T. Unwin. 1984. Molecular structure determination of crystalline specimens in frozen aqueous solutions. *Ultramicrosc.* 13:1–10.

Morozov, S. Y. 1989. A possible relationship of reovirus putative RNA polymerase to polymerases of positive-strand RNA viruses. *Nucleic Acids Res.* 17:5394.

Nibert, M. L., and B. N. Fields. 1992. A carboxy-teminal fragment of protein μl/μ1C is present in infectious subvirion particles of mammalian reoviruses and is proposed to have a role in penetration. *J. Virol.* 66:6408–6418.

Nibert, M. L., T. S. Dermody, and B. N. Fields. 1990. Structure of the reovirus cell-attachment protein: a model for the domain organization of σ1. *J. Virol.* 64:2976–2989.

Nibert, M. L., D. B. Furlong, and B. N. Fields. 1991*a*. Mechanisms of viral pathogenesis. Distinct forms of reoviruses and their roles during replication in cells and host. *J. Clin. Invest.* 88:727–734.

Nibert, M. L., L. A. Schiff, and B. N. Fields. 1991*b*. Mammalian reoviruses contain a myristoylated structural protein. *J. Virol.* 65:1960–1967.

Olson, N. H., and T. S. Baker. 1989. Magnification calibration and the determination of spherical virus diameters using cryo-microscopy. *Ultramicrosc.* 30: 281–298.

Press, W. H., B. P. Flannery, S. A. Teukolsky, and W. T. Vettering. 1989. Linear correlation. *In* Numerical Recipes: The Art of Scientific Computing (FORTRAN version). Cambridge University Press, Cambridge. 484–488.

Ralph, S. J., J. D. Harvey, and A. R. Bellamy. 1980. Subunit structure of the reovirus spike. *J. Virol.* 36:894–896.

Rossmann, M. G., and J. E. Johnson. 1989. Icosahedral RNA virus structure. *Ann. Rev. Biochem.* 58:533–573.

Schiff, L. A., and B. N. Fields. 1990. Reoviruses and their replication. *In* Fields Virology. B. N. Fields and D. M. Knipe, editors. Raven Press, New York. 1275–1306.

Schiff, L. A., M. L. Nibert, M. S. Co, E. G. Brown, and B. N. Fields. 1988. Distinct binding sites for zinc and double-stranded RNA in the reovirus outer capsid protein σ3. *Mol. Cell. Biol.* 8:273–283.

Seliger, L. S., M. Giantini, and A. J. Shatkin. 1992. Translational effects and sequence comparisons of three serotypes of the reovirus S4 gene. *Virology.* 187:202–210.

Silverstein, S. C., and S. Dales. 1968. The penetration of reovirus RNA and initiation of its genetic function in L-strain fibroblasts. *J. Cell Biol.* 36: 197–230.

Smith, R. E., H. J. Zweerink, and W. K. Joklik. 1969. Polypeptide components of virions, top component and cores of reovirus type 3. *Virology.* 39: 791–810.

Strong, J. E., G. Leone, R. Duncan, R. K. Sharma, and P. W. K. Lee. 1991. Biochemical and biophysical characterization of the reovirus cell attachment protein σ1: evidence that it is a homotrimer. *Virology.* 184:23–32.

Sturzenbecker, L. J., M. L. Nibert, D. Furlong, and B. N. Fields. 1987. Intracellular digestion of reovirus particles requires a low pH and is an essential step in the viral infectious cycle. *J. Virol.* 61:2351–2361.

Taylor, K. A., and R. M. Glaeser. 1976. Electron microscopy of frozen hydrated biological specimens. *J. Ultrastruct. Res.* 55:448–456.

Tillotson, L., and A. J. Shatkin. 1992. Reovirus polypeptide σ3 and N-terminal myristoylation of polypeptide μl are required for site-specific cleavage to μlC in transfected cells. *J. Virol.* 66:2180–2186.

Toyoshima, C., and N. Unwin. 1988. Contrast transfer for frozen-hydrated specimens: determination from pairs of defocused images. *Ultramicrosc.* 25:279–292.

Tyler, K. L., R. T. Bronson, K. B. Byers, and B. N. Fields. 1985. Molecular basis of viral neurotropism: experimental reovirus infection. *Neurology.* 35:88–92.

Unwin, N. 1986. The use of cryo-electron microscopy in elucidating molecular design and mechanisms. *Ann. New York Acad. Sci.* 483:1–4.

Virgin, H. W., IV, M. A. Mann, B. N. Fields, and K. L. Tyler. 1991. Monoclonal antibodies to reovirus reveal structure/function relationships between capsid proteins and genetics of susceptibility to antibody action. *J. Virol.* 65:6772–6781.

Weiner, H. L., D. Drayna, D. R. Averill, Jr., and B. N. Fields. 1977. Molecular basis of reovirus virulence: role of the S1 gene. *Proc. Natl. Acad. Sci. USA.* 74:5744–5748.

Weiner, J. R., and W. K. Joklik. 1988. Evolution of reovirus genes: a comparison of serotype 1, 2, and 3 M2 genome segments, which encode the major structural protein μ1C. *Virology.* 163:603–613.

Weiner, J. R., and W. K. Joklik. 1989. The sequences of the reovirus serotype 1, 2, and 3 L1 genome segments and analysis of the mode of divergence of the reovirus serotypes. *Virology.* 169:194–203.

White, C. K., and H. J. Zweerink. 1976. Studies on the structure of reovirus cores: selective removal of polypeptide λ2. *Virology.* 70:171–180.

Yeager, M. J. 1975. Data analysis of low-angle diffraction by one-dimensional crystals. *Brookhaven Symp. Biol.* 27(VII):77–106.

Yeager, M., K. A. Dryden, N. H. Olson, H. B. Greenberg, and T. S. Baker. 1990. Three-dimensional structure of rhesus rotavirus by cryoelectron microscopy and image reconstruction. *J. Cell Biol.* 110:2133–2144.